J|A|C|S
ARTICLES

Structural Characterization of Self-Assembled Multifunctional Binary Nanoparticle Superlattices

Elena V. Shevchenko,*,†,‡,§ Dmitri V. Talapin,†,§ Christopher B. Murray,*,† and Stephen O'Brien‡

Contribution from the IBM Research Division, T. J. Watson Research Center, Nanoscale Materials and Devices, 1101 Kitchawan Road, Yorktown Heights, New York 10598, and Department of Applied Physics & Applied Mathematics, Columbia University, 200 SW Mudd Building, 500 West 120th Street, New York, New York 10027

Received September 18, 2005; E-mail: evshevchenko@lbl.gov; cbmurray@us.ibm.com

Abstract: Nanocrystals of different size and functionality (e.g., noble metals, semiconductors, oxides, magnetic alloys) can be induced to self-assemble into ordered binary superlattices (also known as opals or colloidal crystals), retaining the size tunable properties of their constituents. We have built a variety of binary superlattices from monodisperse PbS, PbSe, $CoPt_3$, Fe_2O_3, Au, Ag, and Pd nanocrystals, mixing and matching these nanoscale building blocks to yield multifunctional nanocomposites (metamaterials). Superlattices with AB, AB_2, AB_3, AB_4, AB_5, AB_6, and AB_{13} stoichiometry with cubic, hexagonal, tetragonal, and orthorhombic symmetries have been identified. Assemblies with the same stoichiometry can be produced in several polymorphous forms by tailoring the particle size and deposition conditions. We have identified arrays isostructural with NaCl, CuAu, AlB_2, $MgZn_2$, $MgNi_2$, Cu_3Au, Fe_4C, $CaCu_5$, CaB_6, $NaZn_{13}$, and *cub*-AB_{13} compounds emphasizing the parallels between nanoparticle assembly and atomic scale crystal growth and providing confidence that many more structures will follow. Recently, we have demonstrated that electrical charges on sterically stabilized nanoparticles in addition to such parameters as particle size ratio and their concentrations can provide the formation of a much broader pallet of binary nanoparticle superlattices[1] as compared with the limited number of possible superlattices formed by hard noninteracting spheres. In this contribution, we demonstrate a large variety of different binary superlattices, provide their detailed structural characterization, and discuss the role of energetic and kinetic factors in the cocrystallization process. We found that Coulomb, van der Waals, charge−dipole, dipole−dipole, and other interactions can contribute equally to cocrystallization, allowing superlattice formation to be dependent on a number of tunable parameters. We present binary superlattices as a new class of materials with a potentially unlimited library of constituents over a wide range of tunable structures.

1. Introduction

Nanoparticles (NPs) and nanocrystalline films are promising candidates for applications ranging from advanced magnetic recording media,[2] light-emitting devices,[3−5] biological tags,[6−8] catalysts,[9−11] solar cells,[12,13] etc. The small size and high surface-to-volume ratio of the individual NPs imparts distinct size tunable physical and electronic properties that have prompted some to refer to them as "artificial atoms". As the number of nanoparticle systems under strict synthetic control has expanded, the parallels to the development of a "new periodic table" have been discussed. The ability to mix and match different NPs and assemble them systematically into ordered binary superlattices, with precisely controlled stoichiometry and symmetry, extends the analogy to multifunctional nanocomposites constituting "nanoparticle compounds". Binary nanocrystal superlattices (BNSLs) raise the possibility of combining the properties of individual components with new properties that arise from the interactions between the nanocrystals. A number of such collective properties arising from the interactions between NPs have already been demonstrated in glassy solids in which the particles have only local order. For example, it has been shown that exchange coupling between nanoparticles of magnetically

---

[†] IBM Research Division.

[‡] Columbia University.

[§] Current address: The Molecular Foundry, Lawrence Berkeley National Laboratory, Berkeley, CA 94720.

(1) Shevchenko, E. V.; Talapin, D. V.; Kotov, N. A.; O'Brien, S.; Murray, C. B. *Nature* **2006**, *439*, 55−59.

(2) Sun, S.; Murray, C. B.; Weller, D.; Folks, L.; Moser. A. *Science* **2000**, *287*, 1989−1992.

(3) Poznyak, S. K.; Talapin, D. V.; Shevchenko, E. V.; Weller, H. *Nano Lett.* **2004**, *4*, 693−698.

(4) Coe, S.; Woo, W.-K.; Bawendi, M.; Bulovic, V. *Nature* **2002**, *420*, 800−803.

(5) Colvin, V.; Schlamp, M.; Alivisatos, A. *Nature* **1994**, *370*, 354−357.

(6) Moronne, M.; Gin, P.; Weiss, S.; Alivisatos, A. P. *Science* **1998**, *281*, 2013−2016.

(7) Nam, J.-M.; Thaxton, C. S.; Mirkin, C. A. *Science* **2003**, *301*, 1884−1886.

(8) Jaiswal, J. K.; Mattoussi, H.; Mauro, J. M.; Simon, S. M. *Nat. Biotechnol.* **2003**, *21*, 47−51.

(9) Narayanan, R.; El-Sayed, M. A. *J. Am. Chem. Soc.* **2003**, *125*, 8340−8347.

(10) Stevens, P. D.; Fan, J.; Gardimalla, H. M. R.; Yen, M.; Gao, Y. *Org. Lett.* **2005**, *7*, 2085−2088.

(11) Narayanan, R.; El-Sayed, M. A. *J. Phys. Chem. B* **2005**, *109*, 12663−12676.

(12) Huynh, W. U.; Dittmer, J. J.: Alivisatos, A. P. *Science* **2002**, *295*, 2425−2427.

(13) Sun, B.; Marx, E.; Greenham, N. C. *Nano Lett.* **2003**, *3*, 961−963.

10.1021/ja0564261 CCC: $33.50

soft and hard materials can enhance the energy product of the nanocomposite material.[14,15] In addition, a significant enhancement of photoluminescence intensity of large semiconductor particles accompanied by quenching of photoluminescence of the small particles[16] was observed in randomly mixed solids of small and large CdSe NPs. This observation is consistent with long-range resonance transfer of electronic excitations from the more electronically confined small particles to higher excited states of the large particles.[16] Also fluorescence, optical absorption, and photocurrent of semiconductor materials were found to be dramatically affected by electromagnetic interactions in the vicinity of the metal surface via the excitation of surface plasmon resonances.[17−19]

In contrast to random mixtures of NPs, the ordered arrays built of two or more types of NPs can provide precise uniformity of packing, stoichiometry, and rigorous control of the interparticle distance. Ordering in a collection of NPs by itself can bring its own exciting properties. It was recently demonstrated that the degree of ordering in 3D superlattices had a pronounced effect on the Raman scattering properties of metal particles. In well-ordered superlattices of Ag NPs, atomic lattices of NPs were found to vibrate coherently.[20]

Monodisperse spherical particles can self-assemble into superlattices with either cubic close-packed (*ccp*) or hexagonal close-packed (*hcp*) packing symmetry.[21,22] Binary mixtures naturally provide a much richer class of compositions and structures. When two types of particles cocrystallize, their individual assembly tendencies must adjust themselves to the properties of space. They must meet, as well as possible, the requirement of certain geometrical principles. Many theoretical studies have been focused on predicting the probability of formation of various ordered binary structures and comparison of their stability.[23−26] In the simplest approach, the formation of a binary assembly is expected only if its packing density exceeds the packing density of single-component crystals in *ccp* or in *hcp* structure (∼0.7405).[27] This space filling principle formulated by Murray and Sanders[27] is still widely used to predict the behavior of particles in binary mixtures. The particle size ratio ($\gamma = R_{\text{small}}/R_{\text{large}}$) and concentrations are considered as the factors determining structure of binary assemblies. Taking into account geometrical considerations, we can predict formation of superlattices isostructural with NaCl, $NaZn_{13}$, and AlB_2. Detailed computer simulations show that the formation of NaCl-, AlB_2-, and $NaZn_{13}$-type structures of hard spheres can be driven by entropy alone without any specific energetic interactions between the particles.[23,25,27] Indeed, $NaZn_{13}$- and AlB_2-type assemblies of silica particles were found in natural Brazilian opals[28,29] and could be grown from latex spheres.[30−32] At the same time, the lattices of hard spheres with CsCl, zinc blende, wurzite structures, as well as any lattices with AB_3, AB_4, or AB_5 stoichiometry are predicted to be unstable for any particle size ratio.[25] To date, there are only several reports demonstrating the possibility of growing BNSLs, that is, the ordered arrays assembled of two different types of NPs.[33−37]

In this contribution, we demonstrate and characterize 16 binary assemblies of NPs with different stoichiometry and packing symmetry. These structures can be reproducibly formed from NPs with different size and functionality (e.g., noble metals, semiconductors, oxides, magnetic alloys). Many structures have the packing fraction density below 0.7405, and their formation is difficult to explain in terms of only entropy-driven crystallization. To explain the observed diversity of BNSLs, we propose a model that demonstrates the importance of Coulomb, van der Waals, charge−dipole, and dipole−dipole interactions for self-assembly of complex nanoparticle superstructures.

2. Experimental Section

2.1. Chemicals. Toluene, ethanol, 2-propanol, squalane, methanol, *n*-hexane, tetrachloroethylene (TCE), oleic acid, $AuCl_3$, AgCl, $AgNO_3$, $PdCl_2$, lead acetate trihydrate, selenium, and bis(trimethylsilyl)sulfide were purchased from Aldrich. Additional chemicals and sources included diphenyl ether (99%, Alfa Aesar), 1,2-hexadecanediol (90%, Fluka), 1-adamantanecarboxylic acid (99%, Fluka), 1,2-dichlorobenzene (99%, Acros Organics), cobalt carbonyl ($Co_2(CO)_8$, stabilized with 1−5% of hexane, Strem), platinum(II)−acetylacetonate ($Pt(acac)_2$, 98%, Strem), hexadecylamine (92%, Merck), and trioctylphosphine (97%, Strem). All chemicals were used as received.

2.2. Nanoparticle Synthesis: All NPs in this work were synthesized in nonpolar solvents and stabilized with amphiphilic molecules containing long (C_{12}−C_{17}) alkyl chains. Detailed information on the preparation of metal, metal oxide, and semiconductor NPs is given below.

2.2.1. Au, Ag, and Pd Nanoparticles. We used a modification of the method developed by Prasad et al. for Au NPs.[38] All reactions were carried out under ambient conditions. In a typical synthesis, metal salt was dissolved in 10 mL of toluene with ultrasonication in the presence of dodecyldimethylammonium bromide (DDAB). For synthesis of 5.0 nm Au, 4.2 and 3.4 nm Ag NPs, we used 0.034 g of $AuCl_3$, 0.025 g of $AgNO_3$, and 0.023 g of AgCl, respectively. The amount of DDAB was 0.0925 g in all three cases; 3.0 nm Pd nanocrystals were synthesized from 0.0237 g of $PdCl_2$ with 0.157 g of DDAB. $AuCl_3$ easily dissolved in the toluene/DDAB mixture forming a clear dark orange solution. $AgNO_3$ and AgCl did not dissolve completely, forming a relatively stable suspension after sonication for ∼30 min. Similarly, partial dissolution of metal salt was observed in case of $PdCl_2$.[39]

Fourty microliters of 9.4 M aqueous solution of $NaBH_4$ was added dropwise to the solution of metal salt with vigorous stirring. One to

---

(14) Zeng, H.; Li, J.; Liu, J. P.; Wang, Z.; Sun S. *Nature* **2002** *420*, 395−398.
(15) Skomski, R.; Coey, J. M. D. *Phys. Rev. B* **1993**, *48*, 15812−15816.
(16) Kagan, C. R.; Murray, C. B.; Bawendi, M. G. *Phys. Rev. B* **1996**, *54*, 8633−8643.
(17) Shimizu, K. T.; Woo, W. K.; Fisher, B. R.; Eisler, H. J.; Bawendi, M. G. *Phys. Rev. Lett.* **2002**, *89*, 117401−1−117401−4.
(18) Kulakovich, O.; Strekal, N.; Yaroshevich, A.; Maskevich, S.; Gaponenko, S.; Nabiev, I.; Woggon, U.; Artemyev, M. *Nano Lett.* **2002**, *2*, 1449−1452.
(19) Schaadt, D. M.; Feng, B.; Yu, E. T. *Appl. Phys. Lett.* **2005**, *86*, 063106−063108.
(20) Courty, A.; Mermet, A.; Albouy, P. A.; Duval, E.; Pileni, A. P. *Nat. Mater.* **2005**, *4*, 395−398.
(21) Murray, C. B.; Kagan, C. R.; Bawendi, M. G. *Science* **1995**, *270*, 1335−1338.
(22) Murray, C. B.; Kagan, C. R.; Bawendi, M. G. *Annu. Rev. Mater. Sci*. **2000**, *30*, 545−610.
(23) Eldridge, M. D.; Madden, P. A.; Frenkel D. *Nature* **1993**, *365*, 35−37.
(24) Eldridge, M. D.; Madden, P. A.; Frenkel, D. *Mol. Phys*. **1993**, *79*, 105−120.
(25) Cottin, X.; Monson, P. A. *J. Chem. Phys.* **1995**, *102*, 3354−3360.
(26) Trizac E.; Eldridge, M. D.; Madden, P. A. *Mol. Phys.* **1997**, *90*, 675−678.
(27) Murray, M. J.; Sanders, J. V. *Philos. Mag. A* **1980**, *42*, 721−740.
(28) Sanders, J. V.; Murray, M. J. *Nature* **1978**, *275*, 201−203.
(29) Sanders, J. V. *Philos. Mag. A* **1980**, *42*, 705−720.
(30) Hachisu, S.; Yoshimura, S. *Nature* **1980**, *283*, 188−189.
(31) Bartlett, P.; Ottewill, R. H.; Pusey, P. N. *Phys. Rev. Lett.* **1992**, *68*, 3801−3804.
(32) Nunt, N.; Jardine, R.; Bartlett, P. *Phys. Rev. E* **2000**, *62*, 900−913.
(33) Redl, F. X.; Cho, K.-S.; Murray, C. B.; O'Brien, S. *Nature* **2003**, *423*, 968−970.
(34) Kiely, C. J.; Fink, J.; Brust, M.; Bethel, D.; Schiffrin, D. J. *Nature* **1998**, *396*, 444−446.
(35) Shevchenko, E. V.; Talapin, D. V.; Rogach, A. L.; Kornowski, A.; Haase, M.; Weller, H. *J. Am. Chem. Soc.* **2002**, *124*, 11480−11485.
(36) Saunders, A. E.; Korgel, B. A. *ChemPhysChem* **2005**, *6*, 61−65.
(37) Shevchenko, E. V.; Talapin, D. V.; O'Brien, S.; Murray, C. B. *J. Am. Chem. Soc.* **2005**, *127*, 8741−8747.
(38) Prasad, B. L. V.; Stoeva, S. I.; Sorensen, C. M.; Klabunde, K. J. *Langmuir* **2002**, *18*, 7515−7520.

two minutes after addition of $NaBH_4$, the color of the reaction mixture turned purple for Au, orange−brownish for Ag, and dark brown for Pd. After 20 min of vigorous stirring, 0.8 mL of 1-dodecanethiol was added, and the stirring of reaction mixture was then continued for 5 more minutes. The NPs formed were precipitated by adding ethanol and isolated by centrifugation. The particles were dried under vacuum, redispersed in 10 mL of toluene in the presence of 0.8 mL of 1-dodecanethiol, and refluxed for 30 min under nitrogen atmosphere to narrow particle size distribution via digestive ripening.[38,40] Then NPs were reprecipitated with 2-propanol and finally redispersed in toluene.

2.2.2. Fe_2O_3 Nanocrystals were synthesized via a modified method of Hyeon et al.[41] Briefly, 11 and 13.6 nm Fe_2O_3 nanocrystals were synthesized by injecting 0.2 mL of iron pentacarbonyl into 10 mL of trioctylamine in the presence of 0.65 g of oleic acid at 270 and 250 °C, respectively. After 20 min of heating at the injection temperature, the reaction temperature was increased to 320 °C. After heating of the reaction mixtures at 320 °C for 1 h, the reaction mixture was cooled to room temperature and 0.17 g of trimethylamine *N*-oxide was added to oxidize iron nanocrystals formed via thermal decomposition of iron pentacarbonyl into γ-Fe_2O_3 nanocrystals.

2.2.3. $CoPt_3$ Nanocrystals: 6.2 nm $CoPt_3$ nanocrystals were prepared by the injection of a cobalt stock solution (0.43 g of $Co_2(CO)_8$ in 0.5 mL of *o*-chlorobenzene) into the solution containing 0.0328 g of Pt-(acac)$_2$, 4 g of hexadecylamine, and 0.25 g of 1-adamantanecarboxylic acid and 2 mL of diphenyl ether preheated at 170 °C. The reaction temperature was kept at 170 °C for 40 min and then increased to 230 °C and kept at this temperature for 30 min (see details in ref 42).

2.2.4. PbSe Nanocrystals: PbSe nanocrystals were synthesized by injecting 18 mL of a 1 M solution of tri-*n*-octylphosphine selenide (TOPSe) in tri-*n*-octylphosphine into the solution of lead oleate heated to 175 °C. The lead oleate solution was prepared by dissolving 2.16 g of $Pb(CH_3COO)_2 \cdot 3H_2O$ in 40 mL of squalane in the presence of 7.3 mL of oleic acid followed by drying and degassing under vacuum at 80 °C for 1 h. Immediately after injection of TOPSe, the reaction mixture was cooled to ∼150 °C, and this temperature was maintained for further NP growth. Aliquots of the crude solution were taken at different time intervals (1−10 min) to obtain samples of PbSe nanocrystals of different sizes. The aliquots of crude solution were mixed with an equal volume of hexane, and the PbSe nanocrystals were precipitated by adding anhydrous ethanol. Details of the synthesis can be found in ref 43.

2.2.5. PbS Nanocrystals were synthesized from lead oleate and bis-(trimethylsilyl)sulfide with oleic acid as the capping ligand. Details of the synthesis can be found in ref 44.

2.3. Preparation of Binary Assemblies: Substrates (e.g., TEM grids or silcon nitride membranes) were placed in a glass vial containing colloidal solution of NPs. The vial was tilted by 60−70° and placed inside a low-pressure chamber as shown in Figure 1. Ordered binary assemblies formed upon evaporation of the solvent. Toluene and mixtures of toluene with tetrachloroethylene or chloroform were used as solvents (∼1:1 by volume). The best BNSLs (as determined by length scale of ordering and low occurrence of defects) were obtained by evaporating relatively concentrated colloidal solutions at 45 °C under reduced pressure (∼3.2 kPa). The increased temperature was essential for better solubility of Au, Ag, and Pd NPs as these tend to show some flocculation at room temperature.[38,45]

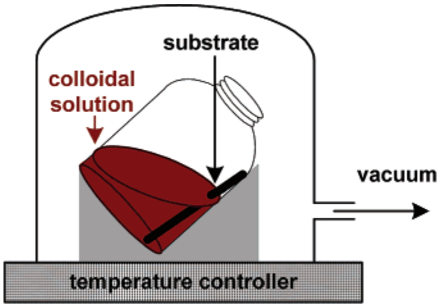

Figure 1. A scheme of the low-pressure chamber used for growing ordered binary assemblies.

We studied the effect of various substrates on the growth of BNSLs. The BNSLs can be reproducibly grown on hydrophobic substrates, such as amorphous carbon and silicon nitride substrates, in contrast to OH-terminated silicon oxide and other hydrophilic substrates, for which mostly amorphous or phase-segregated solids were observed.

3. Results and Discussion

3.1. Nanoparticle Characterization and Classification of the Symmetry of the Binary Superstructures. Nanoparticles used in this work were sterically stabilized with hydrophobic molecules containing long alkyl chains. We measured average nanoparticle size and thickness of the organic stabilizer shell by routine TEM investigations of single-component monolayers. TEM analysis of Ag and Pd NPs stabilized by dodecanethiol showed an interparticle spacing of ∼1.7 nm. This value is significantly smaller than the 2-fold thickness of a dodecanethiol monolayer and is in good agreement with the effective thickness of the dodecanethiol shell reported for Ag NPs by Korgel et al.[46] In measuring the interparticle spacing for a large series of samples, we observe some deviation (∼0.2 nm) in the average interparticle spacing for different samples with the same capping group. The effective thickness of the ligand shell could vary slightly from sample to sample, depending on surface coverage and radius of curvature and possible small variations in extraneous organic material left after the purification process. The spacing between the neighbors in a close-packed nanoparticle array is set by the balance of repulsive steric and attractive van der Waals forces.[46] Table 1 summarizes dimensions of NPs we have used as building blocks to create our BNSLs. In the remainder of this work, we use the term “effective particle size” to describe the nanoparticle size relevant for packing, which is the sum of crystalline core diameter and twice the effective thickness of the ligand shell. The ratio of effective particle sizes between “small” and “large” particles will be further referred to as “effective size ratio”.

To aid structural analysis, the BNSLs were generally grown on electron transparent substrates (amorphous carbon film, silicon nitride membranes). Samples displayed lateral ordering over distance up to 10 μm. Regions of the nanoparticulate sample 1−5 layers thick provided the best imaging, while real space investigation of regions thicker than 5 layers was

---

(39) We believe that the presence of nondissolved metal salt during nucleation and growth of nanoparticles allows the concentration of metal precursors to be kept at nearly constant level. This should be favorable for narrow final particle size distribution. For example, the use of highly soluble palladium acetate instead of $PdCl_2$ resulted in more polydisperse Pd nanoparticles with similar mean size.

(40) Prasad, B. L. V.; Stoeva, S. I.; Sorensen, C. M.; Klabunde, K. J. *Chem. Mater.* **2003**, *15*, 935−942.

(41) Hyeon, T.; Lee, S. S.; Park, J.; Chung, Y.; Na, H. B. *J. Am. Chem. Soc.* **2001**, *123*, 12798−12801.

(42) Shevchenko, E. V.; Talapin, D. V.; Schnablegger, H.; Kornowski, A.; Festin, O.; Svedlindh, P.; Haase, M.; Weller, H. *J. Am. Chem. Soc.* **2003**, *125*, 9090−9101.

(43) Cho, K.-S.; Talapin, D. V.; Gaschler, W.; Murray, C. B. *J. Am. Chem. Soc.* **2005**, *127*, 7140−7147.

(44) Hines, M. A.; Scholes, G. D. *Adv. Mater.* **2003**, *15*, 1844−1849.

(45) The stability of the colloidal solutions was monitored by measuring angle-dependent scattering of monochromic light (363 nm) at different temperatures. It was found that Au, Ag, and Pd NPs had a tendency to form aggregates at room temperature, while at temperatures above 40 °C, no aggregation was observed.

(46) Korgel, B. A.; Fullam, S.; Connolly, S.; Fitzmaurice, D. *J. Phys. Chem. B* **1998**, *102*, 8379−8388.

Table 1. Nanoparticles Used as Building Blocks for BNSLs

NPs	size of crystalline core (nm)	std. %	capping ligand	effective thickness of ligand shell[a] (nm)
Pd	3.0	7	dodecanethiol	0.85
Ag	3.4	8		
	3.6	7		
	4.2	6		
Au	5	7		0.75
PbSe	5.8	5	oleic acid	0.9
	6.2	5		0.85
	7.2	6		
	7.6	5		
$CoPt_3$	6.2	7	ADA, HDA[b]	1
PbS	6.7	5	oleic acid	0.85
γ-Fe_2O_3	13.4	6		0.9

[a] Defined as half the interparticle spacing in the (111) projection of close-packed 2D nanoparticle superlattices. [b] ACA is 1-adamantanecarboxylic acid, HDA is hexadecylamine.

prevented by limited electron penetration. A Philips CM12 microscope operating at 120 kV was used for all imaging. Surveys of electron diffraction and high-resolution SEM confirm that ordering can persist in thick nanoparticulate films.

Three-dimensional descriptions of the superlattices were developed by surveying large regions of the samples, to categorize all the crystal orientations, and recording a series of 2D projections down the major symmetry axes. Tilting of the samples allowed observation of additional orientations not expressed in the plane view images of the films. In many cases, the analysis of a series of these 2D lattice projections resulted in a single-crystal structure. To assign the observed structures to crystallographic space groups, we built 3D lattice models for the 180 most common space groups using Accelrys MS Modeling 3.1 software. The TEM images were compared with simulated projections to match the symmetry of our superlattices. We also performed a comparison of experimental small-angle electron diffraction patterns taken over larger areas, and the 2D Fourier transformation power spectra of real space TEM images and the FFT power spectra of the simulated projections to ensure consistency.

3.2. Binary Superlattices with AB Stoichiometry. 3.2.1. AB Superlattices Isostructural with NaCl. The NaCl lattice (SG 225, $Fm\bar{3}m$) has the highest packing density (0.793 at $\gamma = 0.414$) among the binary lattices with AB stoichiometry. The packing density of the NaCl-type lattice exceeds the packing density of *fcc* close-packed spheres for all size ratios γ below 0.458.[27] Kiely et al. earlier reported observation of small 2D arrays (about 40 nm across a domain) of a NaCl-type superlattice for Au and Ag NPs.[47] Recently, Korgel et al. reported the NaCl-type superlattice of Fe and Au nanoparticles over more extended areas (~0.3 μm^2).[36] Here we report the NaCl-type superlattices for various combinations of NPs, such as 13.4 nm Fe_2O_3 − 5.0 nm Au, 7.2 nm PbSe − 3.0 nm Pd, and 5.8 nm PbSe − 3.0 nm Pd, with each ordered domain extending over several microns (Figure 2). In the Fe_2O_3 − Au and 7.2 nm PbSe − 3.0 nm Pd systems, the NaCl superlattices are usually represented by (111) projections (Figure 2a). Typically, domains consisted of two layers of large Fe_2O_3 particles and two layers of small Au particles (Figure 2a, cf. Figure 2a and 2g and Figure 2b and 2g). Smaller domains of (100) projections of NaCl-type superlattices were also observed (Figure 2a,b, upper insets). In the case of PbSe−Pd systems, the (100) oriented NaCl superlattices dominated (Figure 2b). The NaCl-type ordering was observed for NPs with effective size ratios of 0.43, 0.528, and 0.62 for 13.4 nm Fe_2O_3 − 5.0 nm Au, 7.2 nm PbSe − 3.0 nm Pd, and 5.8 nm PbSe − 3.0 nm Pd, respectively. All these values are above the range of stability predicted for NaCl superlattices of hard noninteracting spheres (Table 2).

Table 2. Maximum Packing Density and Range of Stability Calculated for Binary Lattices of Hard Spheres

stoichiometry	type of structure	maximum packing density (γ)	range of stability	ref
AB	NaCl	0.793 (0.414)	below 0.458	27
			$0.2 \leq \gamma \leq 0.42$	25
	NiAs	0.793 (~0.4)	~0.4	59
	CsCl	0.729, unstable	0.732	60
AB_2	AlB_2	0.778(0.58)	$0.482 \leq \gamma \leq 0.624$	27
			$0.42 \leq \gamma \leq 0.59$	25
	Laves phases; hexagonal: $MgZn_2$, $MgNi_2$ cubic $MgCu_2$	0.71 (0.813) unstable	$0.606 \leq \gamma \leq 0.952$	27
	CaF_2	0.757 unstable	0.225	25
AB_{13}	$NaZn_{13}$ (*ico*-AB_{13})	0.738 (0.58)	$0.54 \leq \gamma \leq 0.61$	25
			$0.474 \leq \gamma \leq 0.626$	23,24
	ico-AB_{13}, with some size distribution for B spheres	above 0.755	$0.537 \leq \gamma \leq 0.583$	27
	cub-AB_{13}	0.700 (0.565)	unstable	27

3.2.2. AB Superlattices Isostructural with CuAu Phase. The BNSLs crystallize from solutions of 7.6 nm PbSe and 5 nm Au NPs, 5.8 nm PbSe and 3.4 nm Ag NPs, as well as 6.2 nm PbSe and 5 nm Au NPs mixed with the concentration ratio of 1:3−1:5 (Figure 3). The lateral dimensions of superlattice domains formed on TEM grids can approach ~3 μm × 3 μm (i.e., ~10 μm^2), while the superlattice thickness usually does not exceed 4−6 NPs. Figure 3a,b,d and 3c,k shows two different projections of the superstructure we assigned as the (001) and (100) projections of tetragonal CuAu lattice (SG 123, $P4/mmm$), correspondingly. The TEM projection of the (001) plane of the AuCu lattice is similar to the projection of the (100) plane of the CaF_2 lattice (Supporting Information, Figure S1). To reveal whether the superlattices shown in Figure 3 correspond to AuCu or CaF_2 symmetry, we performed TEM tilting experiments. The cubic CaF_2 lattice tilted by 45° should orient along the (110) zone axis, while tetragonal CuAu lattice shows no zone axes at any tilt smaller than 90°. The tilting experiments revealed no characteristic periodic patterns at 45° tilt, which allowed us to assign the structure shown in Figure 3a,b,d to CuAu phase. The TEM images shown in Figure 3c,k can be unambiguously assigned to the (100) projection of the AuCu lattice with characteristic alternating lines of large and small particles (note that (100) and (010) planes are equivalent). These lines correspond to the planes consisting of large and small NPs that alternate along the ⟨001⟩ direction. The superlattice patterns shown in Figure 3a,c usually coexist on a single TEM grid, supporting our conclusion that these different projections belong to the same structure. Depending on particular particle combinations, the occurrence of (100) and (001) projections can vary. The (001) projections dominate for PbSe−Au NP superlattices,

---

(47) Kiely, C. J.; Fink, J.; Zheng, J. G.; Brust, M.; Bethell, D.; Schiffrin, D. J. *Adv. Mater.* **2000**, *12*, 640−643.

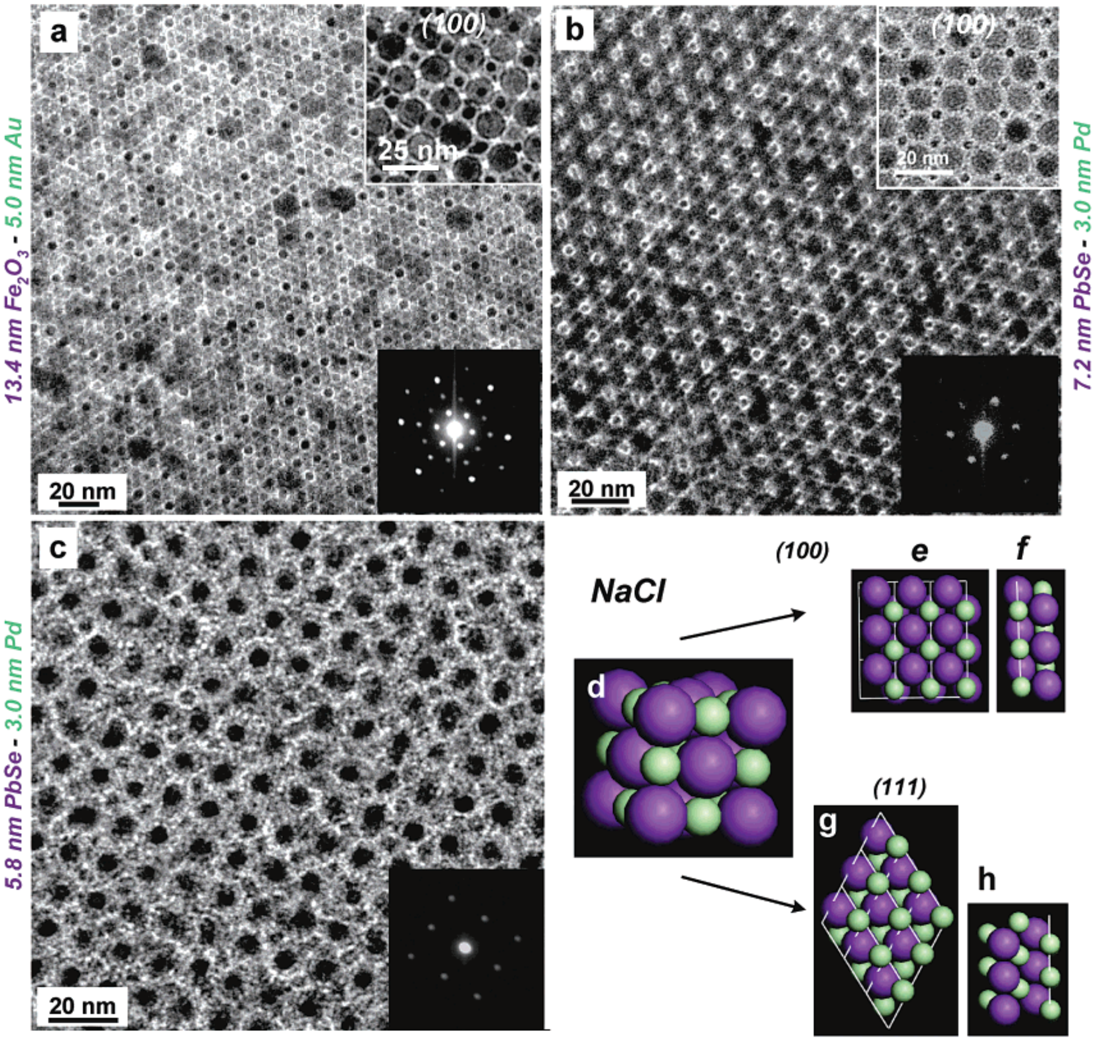

Figure 2. TEM micrographs of NP superlattices isostructural with NaCl: (a, b) The (111) projection formed by 13.4 nm Fe_2O_3 and 5.0 nm Au NPs and 7.2 nm PbSe and 3.0 nm Pd NPs; upper insets shows the (100) projections of the superlattice formed by the same NPs. (c) The (100) projection formed by 5.8 nm PbSe and 3.0 nm Pd NPs. Bottom insets in (a), (b), and (c) show small-angle ED patterns measured from corresponding superlattices. (d) Three-dimensional sketch of NaCl unit cell. (e, g) Depictions of the (100) and (111) planes, respectively. (f, h) Depictions of minimum number of layers in the (100) and (111) projections necessary for the formation of the patterns identical with the observed ones. The (100) plane in the case of 7.2 nm PbSe and 3.0 nm Pd NPs was represented by a monolayer, consisting of large and small NPs.

and (100) projections represent the majority for PbSe−Ag superlattice samples.

The CuAu-type structure was observed for numerous intermetallic compounds.[47] In the CuAu lattice, each particle is surrounded by four identical particles and eight of the second component. The effective size ratio of NPs that assemble into CuAu-type superlattices is usually in γ-range of ∼0.55−0.70. These values are considerably smaller than size ratios reported for intermetallic compounds with CuAu lattice.[48] The CuAu-type BNSLs usually coexist with Cu_3Au-type superlattices (see below).

Within a certain temperature range (380 °C < T < 410 °C), CuAu intermetallic compounds show characteristic periodic arrangement of antiphase boundaries along the ⟨100⟩ axis.[48] These antiphase boundaries are separated by several unit cells, as shown in Figure 3m. We observed similar phenomenon for colloidal binary superlattices. The most pronounced antiphase boundaries were observed for CuAu BNSLs with the smallest particle size ratio, 6.7 nm PbS − 3.0 nm Pd, $\gamma \sim 0.56$ (Figure 3l,n). Probably, the antiphase domains form to release the lattice strain energy associated with the deviation of particle size ratio from the most energetically favorable values.

3.2.3. AB Superlattices with Orthorhombic Symmetry. Another novel superstructure was formed by slowly evaporating the mixture of 5.8 nm PbSe and 3 nm Pd NPs and 7.2 nm PbSe and 4.2 nm Ag NPs (particle concentration ratio ∼1:3). The typical area of single-crystalline domains was ∼0.5−1 μm^2. Figure 4a,c shows TEM images of two characteristic superlattice projections. Using Accelrys software (MS Modeling 3.1), we modeled this structure and assigned it to the orthorhombic symmetry class (SG 51, *Pmma*). The projections shown in Figure 4a,b,i and 4c,j are in good agreement with (100) and (010) projections of the proposed orthorhombic structure. The proposed structure belongs to the same space group as the AuCd intermetallic compound; however, they do not appear to be isostructural.

---

[48] Barrett, C.; Massalski, T. B. *Structure of Metals*, 3rd ed. International Series on Materials Science and Technology; Pergamon Press: New York, 1987; Vol. 35, pp 279−284.

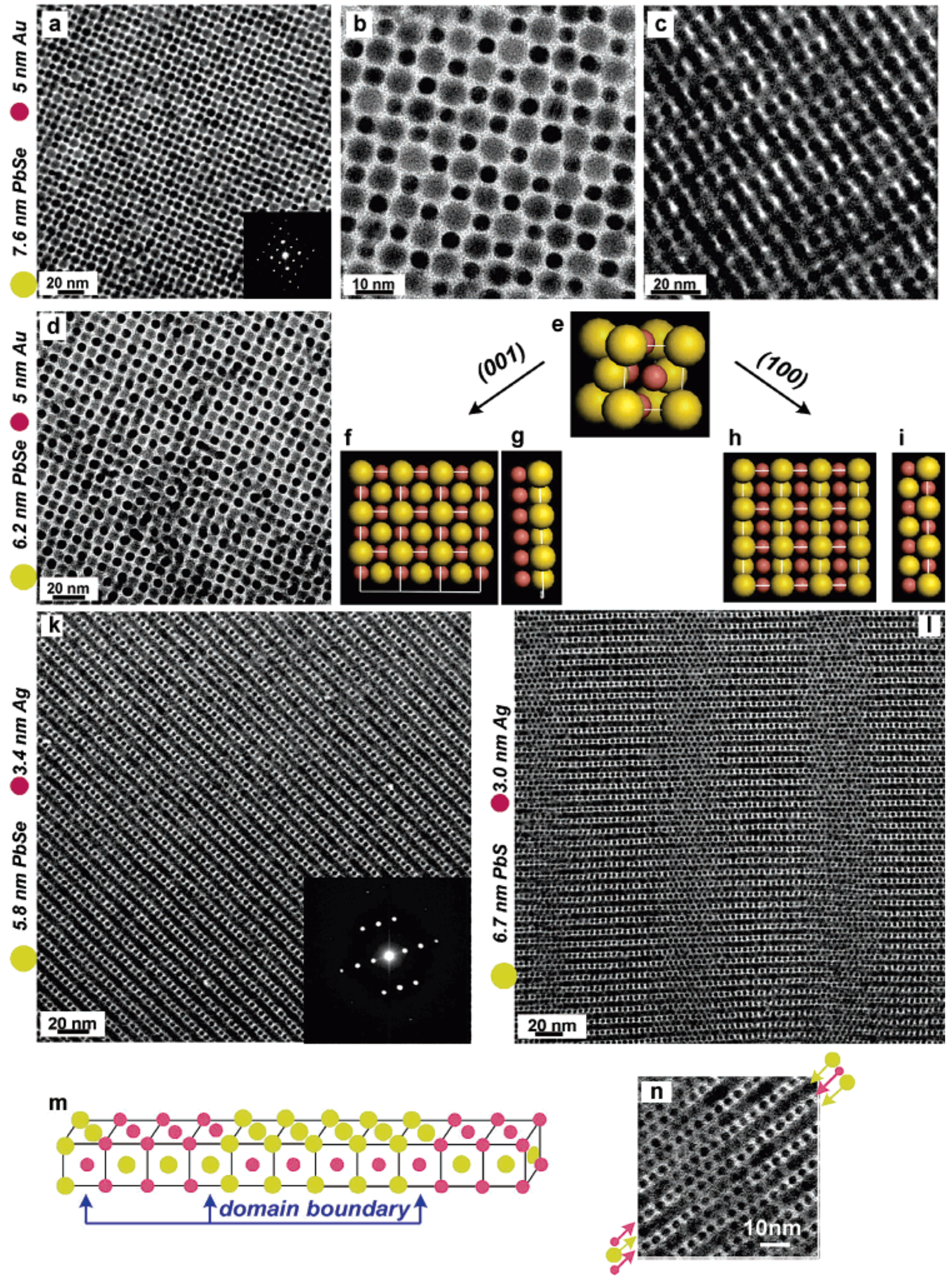

Figure 3. TEM micrographs of BNSL isostructural with AuCu formed by 7.6 nm PbSe and 5.0 nm Au NPs: (a) TEM overview of the (001) projection; (a, inset) small-angle ED pattern of the (001) plane; (b) as in (a) but at high magnification; (c) TEM overview of the (100) plane. TEM micrographs of AuCu-type BNSL formed by 6.2 nm PbSe and 5.0 nm Au NPs; (e) 3D sketch of the AuCu unit cell (SG 123, *P*4/*mmm*). (f, h) Depictions of the (001) and (100) planes, respectively. (g, i) Depictions of minimum number of layers in the (001) and (100) planes, respectively, leading to the formation of the patterns identical with the observed ones. (k) TEM micrograph of the (100) projection of AuCu-type BNSL formed by 5.8 nm PbSe and 3.4 nm Ag NPs. Inset in (i): small-angle ED pattern measured from the (100) plane. (l, m) TEM images of the (100) projection containing nanoparticle "antiphases". (m) Depiction of an antiphase boundary.

3.3. Binary Superlattices with AB$_2$ Stoichiometry. 3.3.1. AB$_2$ Superlattices Isostructural with AlB$_2$. We observed formation of AB$_2$ superstructures isostructural with AlB$_2$ (SG 191, *P*6/*mmm*) from different nanoparticle building blocks. The AlB$_2$-type structure is based on a hexagonal unit cell. The (001) projections are usually observed in plane view TEM. The characteristic features of this structure are hexagons formed by small and large NPs tilted by 30° with respect to each other. Figure 5 shows the (001) projections of AlB$_2$-type superlattices assembled from different combinations of NPs (semiconductor−noble metal, semiconductor−magnetic material, magnetically hard−magnetically soft materials). Small-angle electron diffraction patterns demonstrate the long-range order in such structures (insets to Figure 5a,c,d). The (110), (011), and (111) projections of the AlB$_2$-type superlattice assembled from 5.8 nm PbSe and 3.0 nm Pd NPs are shown in Figure 6.

Murray and Sanders predicted on the basis of optimum space-filling that AlB$_2$-type structure should be stable for γ in range of 0.482−0.624.[27] The effective size ratios for superstructures shown in Figure 4 are 0.71, 0.56, 0.54, 0.5, and 0.787 for PbSe−Ag, PbS−Pd, CoPt$_3$−Fe$_2$O$_3$, Fe$_2$O$_3$−PbSe, and PbSe−Au, respectively. The values 0.71 and 0.787 significantly exceed

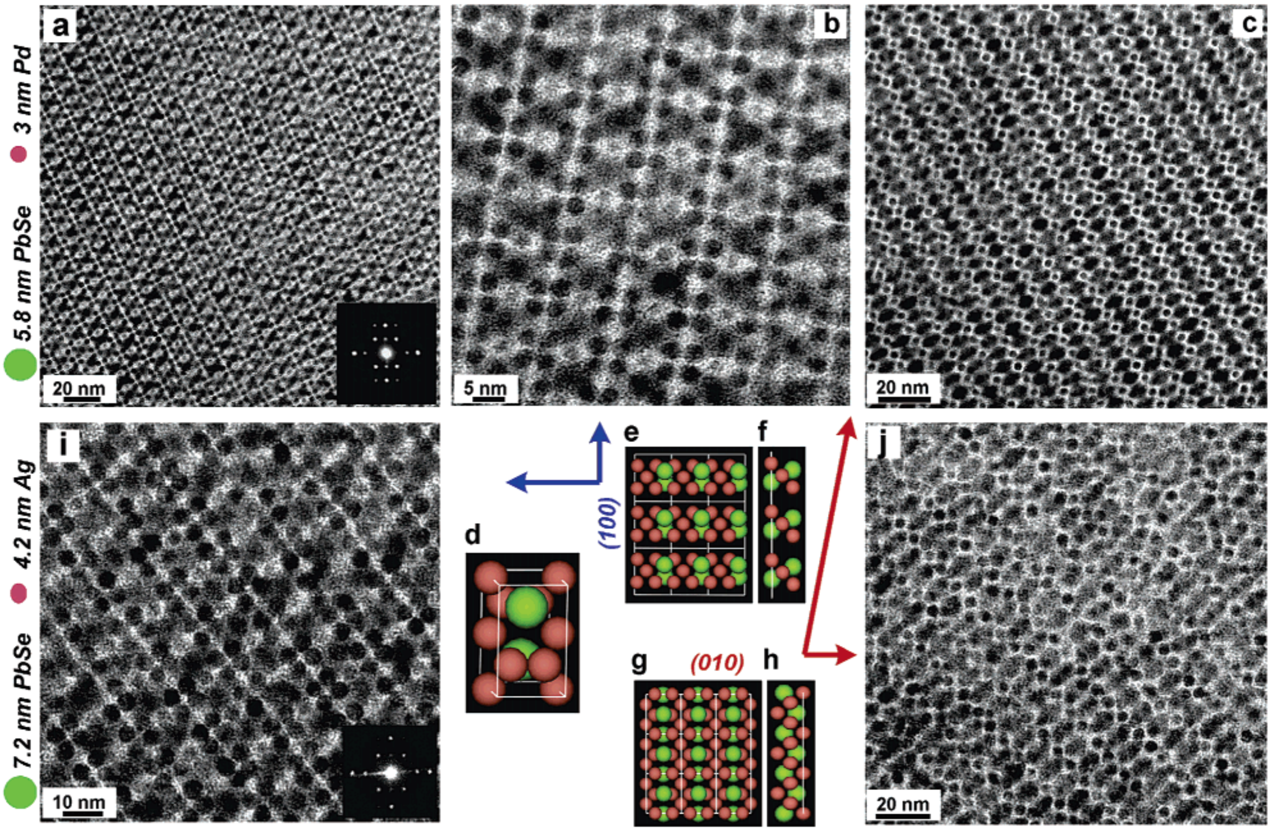

Figure 4. TEM micrographs of orthorhombic BNSL formed by 5.8 nm PbSe and 3.0 nm Pd NPs: (a, b) (100) projection; (a, inset) a small-angle ED pattern; (c) (010) projection. (d) Three-dimensional sketch of proposed orthorhombic lattice (SG51, *Pmma*). (e, f) Depictions of the (100) and (010) planes, respectively. (g, h) Depictions of minimum number of layers in the (100) and (010) planes, respectively, leading to the formation of the patterns identical with the observed ones. (i, j) TEM micrographs of the (100) and (010) projections of orthorhombic BNSL, formed by 7.2 nm PbSe and 4.2 nm Pd NPs; (i, inset) a small-angle ED pattern.

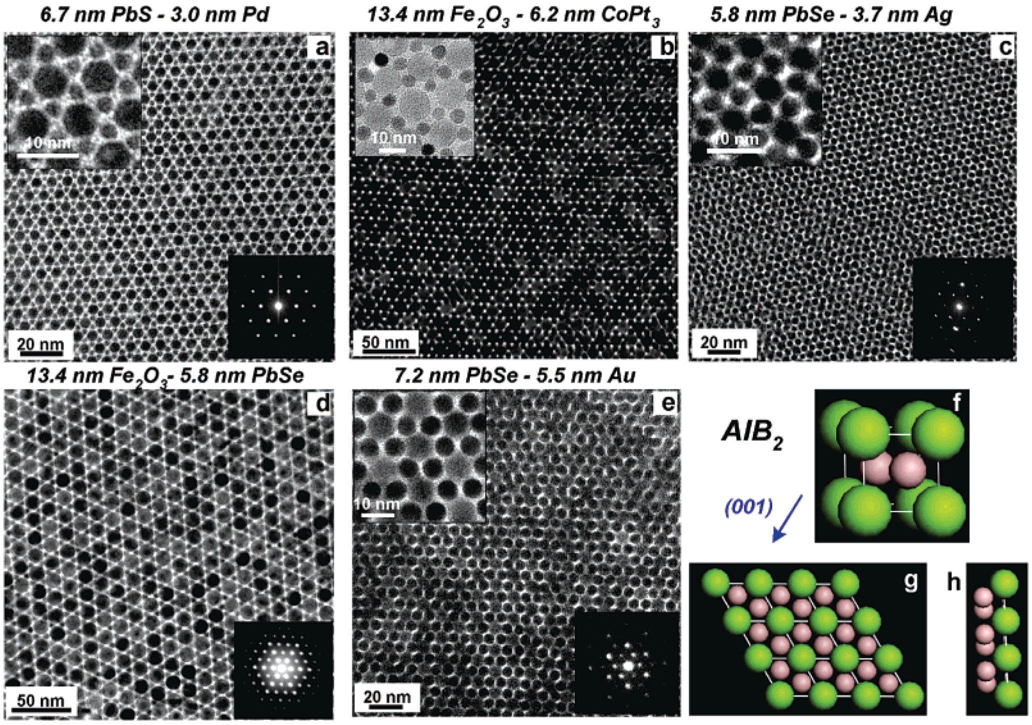

Figure 5. TEM micrographs of the (001) planes of BNSL isostructural with AlB$_2$ formed by (a) 6.7 nm PbSe and 3.0 nm Pd NPs, (b) 13.4 nm Fe$_2$O$_3$ and 6.2 nm CoPt$_3$ NPs, (c) 5.8 nm PbSe and 3.7 nm Ag NPs, (d) 13.4 nm Fe$_2$O$_3$ and 5.8 nm PbSe NPs, and (e) 7.2 nm PbSe and 5.5 nm Au NPs. Top left insets in (a), (b), (c), and (e) show a closer look of the arrangement of NPs in the AlB$_2$-type superlattice. Right bottom insets in (a), (c), (d), and (e) show small-angle ED patterns measured from the (001) plane. (f) Three-dimensional sketch of AlB$_2$ unit cell. (g) Depiction of the the (001) plane. (h) Depiction of minimum number of layers in the (001) plane, leading to the formation of the patterns identical to the observed ones.

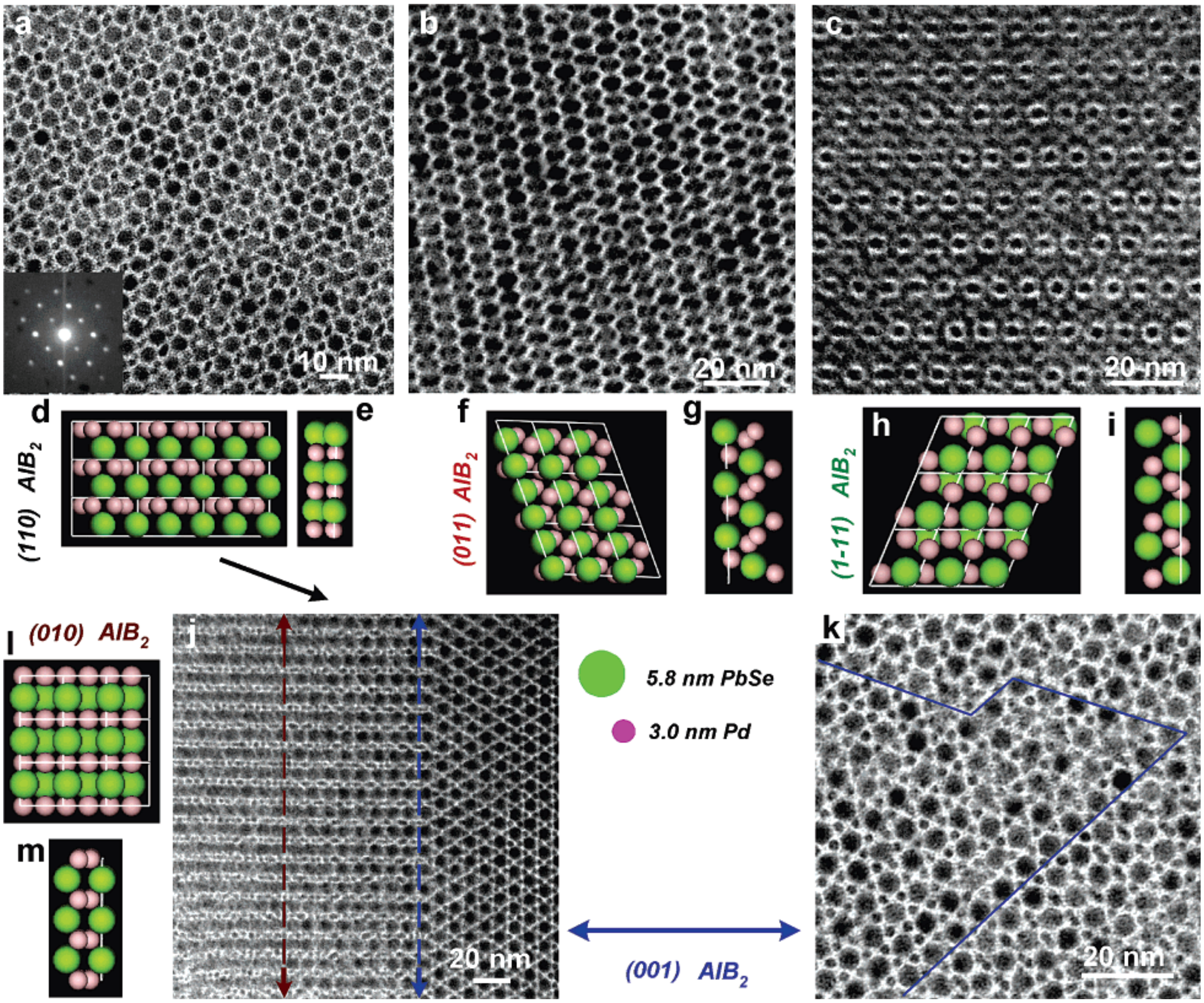

Figure 6. TEM micrographs of BNSL isostructural with AlB_2 (SG 191, *P*6/*mmm*) formed by 5.8 nm PbSe and 3.0 nm Pd NPs. Overview of (a) (110), (b) (011), and (c) (111) projections. (a, inset) Small-angle ED pattern from the (110) plane. (d, f, h, l) Depictions of the (110), (011), (111), and (1 −1 1) planes, respectively. (e, g, i, m) Depictions of minimum number of layers in the (110), (011), and (111) planes, respectively, leading to the formation of the patterns identical to the observed ones. (j, k) TEM micrographs displaying the grain boundary between (010) − (110) − (001) and (110) − (001) oriented planes.

the maximum size ratio predicted for a stable AlB_2-type structure. As a possible explanation, the nanoparticle superlattice could tolerate a broader range of γ values by rearranging the soft shells of organic ligands in a way that favors formation of a dense binary assembly. For example, local interdigitation of alkyl chains can significantly affect effective particle size.

3.3.2. AB_2 Superlattices Isostructural with Hexagonal Laves Phases ($MgZn_2$ and $MgNi_2$). Figure 7a,b shows the TEM images of ordered binary superlattices with characteristic features resembling "radiation signs". This superlattice self-assembled from 6.2 nm PbSe and 3.0 nm Pd NPs. Modeling of the TEM images allowed us to assign this structure to one of the hexagonal Laves phases. Small-angle electron diffraction pattern confirms hexagonal symmetry of the superlattice projection (Figure 7a, inset). The superlattice projection shown in Figure 7a,b is in good agreement with the (001) projection of the $MgZn_2$ lattice (Figure 7c−e). $MgZn_2$-type Laves phases have been observed in intermetallides and in so-called "solid van der Waals compounds" such as $CH_4(H_2)_2$[49] and $Ar(H_2)_2$[50] that are stable at a high pressure.

The $MgZn_2$-type structure contains four formula units per cell and belongs to the space group $P6_3/mmc$ (SG 194). In this structure, the smaller nanoparticles are arranged in tetrahedra, and these tetrahedra are joined alternately base-to-base and point-to-point. The larger NPs fit into the holes enclosed by tetrahedra. The ratio of atomic radii is considered as a structure-determining factor in the formation of Laves phases in intermetallic alloys.[51] In Laves phases, the highest packing density of 0.71 corresponds to $\gamma \sim 0.813$.[27] For different intermetallic compounds, the ratio of atomic radii can vary from 0.606 to 0.952.[51] The effective size ratio of Pd and PbSe NPs is ∼0.6, which is close to the low limit of size ratio acceptable for $MgZn_2$-type intermetallic compounds.

The domains of the $MgZn_2$-type superlattice usually coexist with the other crystalline binary phases. We assigned this structure to $MgNi_2$-type shown in Figure S2 in the Supporting Information. $MgNi_2$-type structure represents another hexagonal Laves phase and belongs to the same space group as $MgZn_2$. The stacking sequences in $MgZn_2$ and $MgNi_2$-type crystalline

---

(49) Somayazulu, M. S.; Finger, L. W.; Hemley, R. J.; Mao, H. K. *Science* **1996**, *271*, 1400−1402.

(50) Loubeyre, P.; Letoulecc, R.; Pinceaux, J.-P. *Phys. Rev. Lett.* **1994**, *72*, 1360−1363.

(51) Wernick, J. H. In *Intermetallic Compounds*; Westbrook, J. H., Ed.; Robert E. Krieger Publishing Company: Malabar, FL, 1977; pp 198−204.

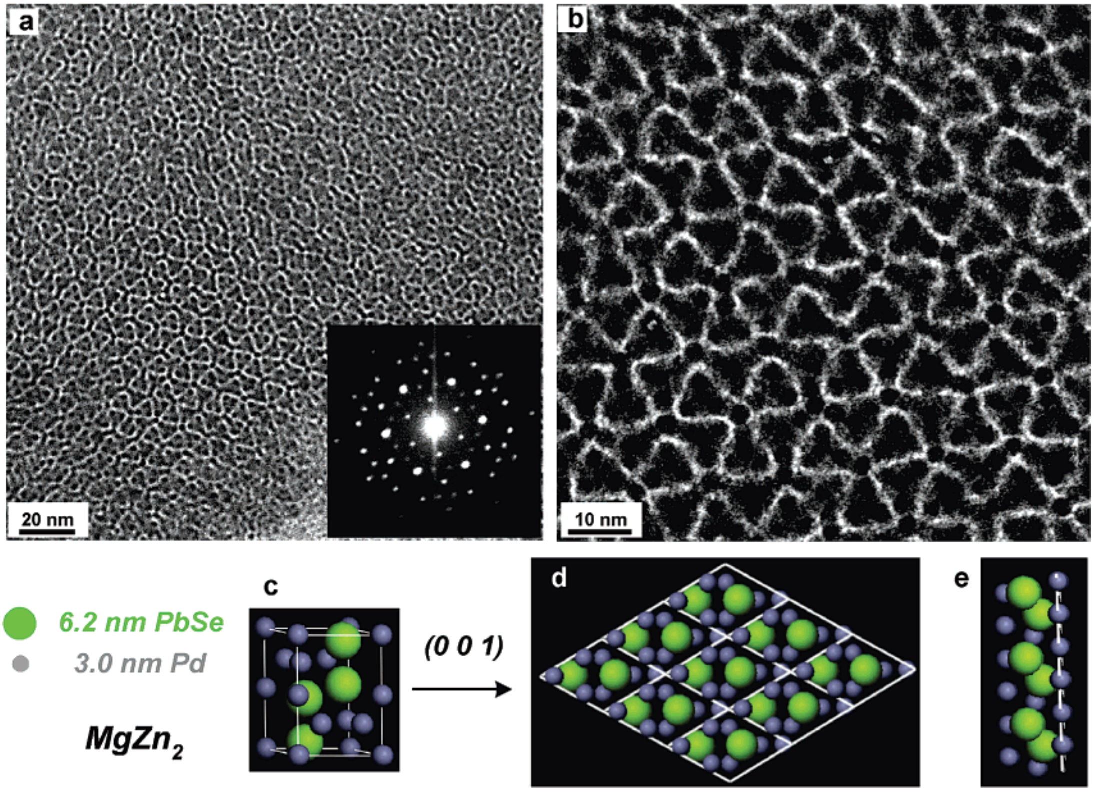

Figure 7. TEM micrographs of superlattices isostructural with $MgZn_2$ formed by 6.2 nm PbSe and 3.0 nm Pd NPs: (a) TEM overview of the (001) plane; (a, inset) Small-angle ED pattern from the (001) plane. (b) As (a) but at high magnification; (c) 3D sketch of the $MgZn_2$ unit cell (SG 194, $P6_3/mmc$). (d) Depictions of the (001) plane. (e) Depictions of minimum number of layers in the (001) planes that needed to reproduce those observed experimentally.

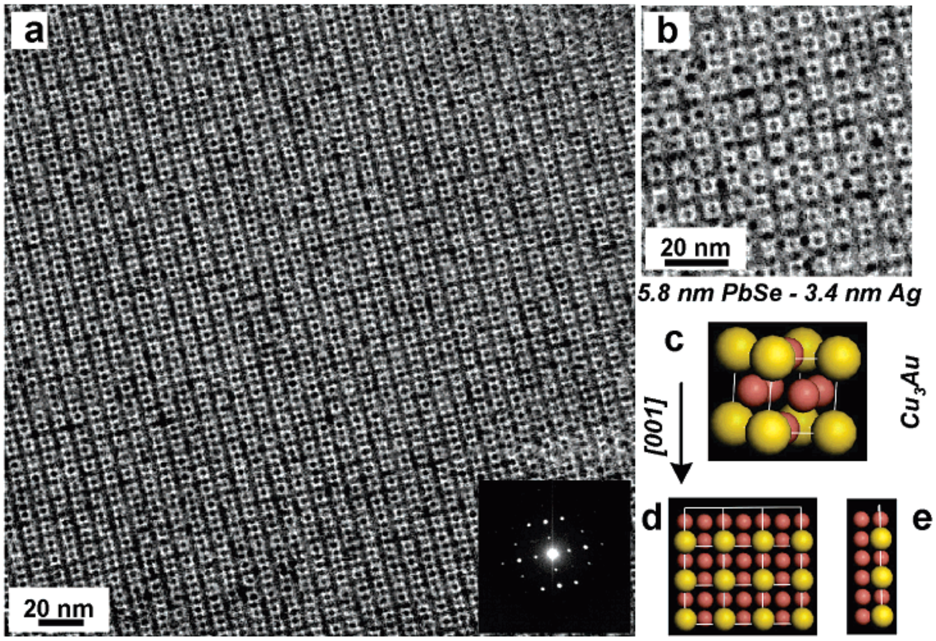

Figure 8. TEM micrographs of superlattices isostructural with Cu_3Au (SG 221, $Pm\bar{3}m$) formed by 5.8 nm PbSe and 3.4 nm Ag NPs: (a, b) TEM images of the (001) projection, (a, inset) small-angle ED pattern of the (001) plane; (c) 3D sketch of the Cu_3Au unit cell. (d) Depiction of the (001) projection. (e) Depictions of minimum number of layers in the (001) projection leading to the patterns identical to the observed ones.

structures are ABABAB... and ABACABAC..., respectively. $MgNi_2$ structure contains eight formula units per cell (Figure S2 from Supporting Information).

3.4. Binary Superlattices with AB_3 Stoichiometry Isostructural with Cu_3Au. Superlattices isostructural with the cubic Cu_3Au intermetallic compounds (SG 221, $Pm\bar{3}m$) can self-assemble from a mixture of 5.8 nm PbSe and 3.4 nm Ag NPs stabilized by oleic acid and dodecanethiol, respectively (the particle concentration ratio ∼1:7). Figure 8a,b shows the (001) projection of the Cu_3Au-type superlattice. The thickness of the superlattice typically varied between 2 and 4 layers of NPs.

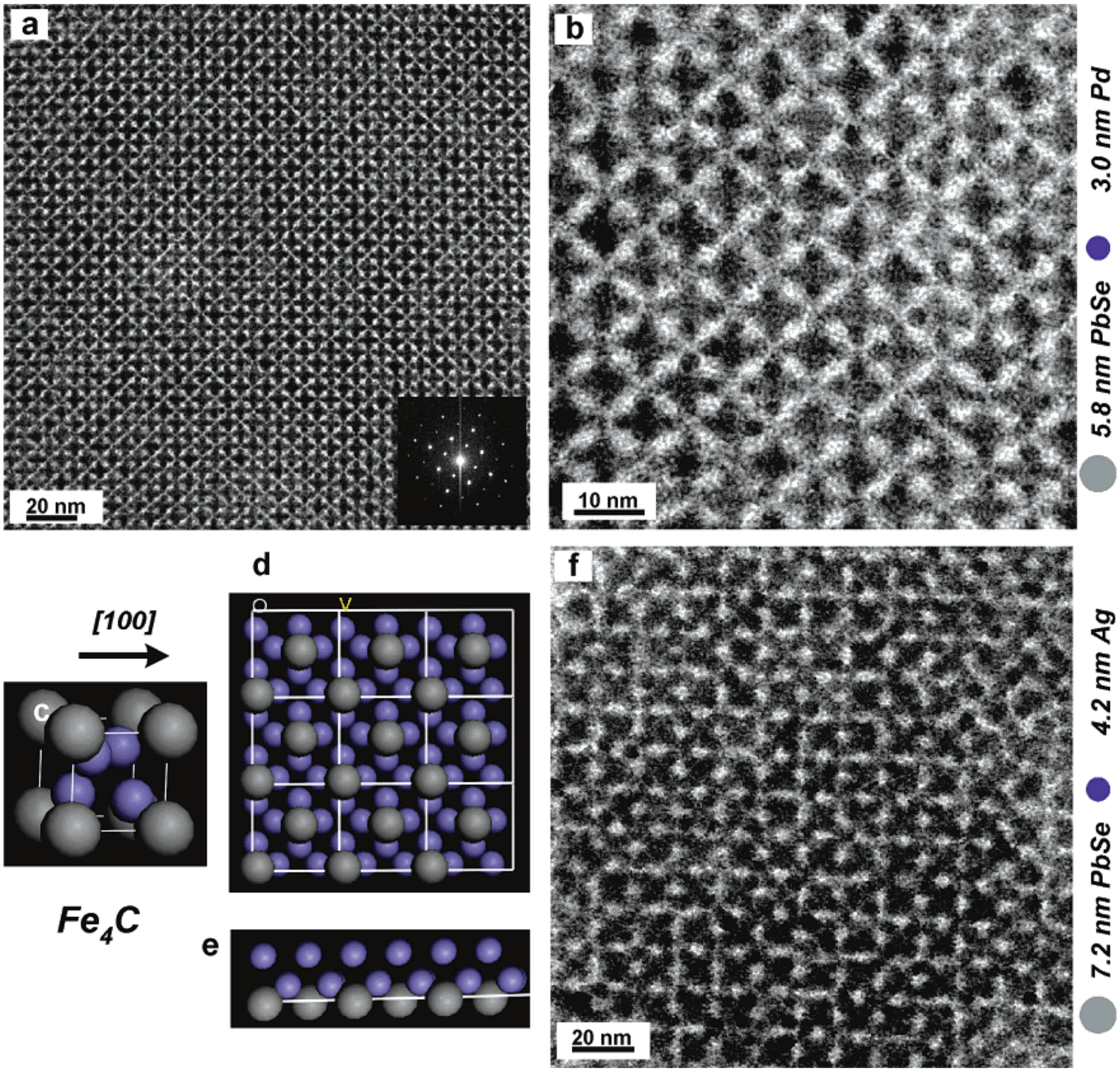

Figure 9. (a, b) TEM images of (100) projections of BNSL isostructural with Fe_4C formed by 5.8 nm PbSe and 3.0 nm Pd NPs; (a, inset) small-angle ED pattern of the (100) projection. (c) Three-dimensional sketch of the Fe_4C unit cell. (d) Depiction of the (100) projection. (e) Depictions of minimum number of layers in the (100) projection leading to the patterns identical to the observed ones. (f) TEM micrograph of the (100) projection of Fe_4C-type BNSL consisting of 7.2 nm PbSe and 4.2 nm Ag NPs.

3.5. Binary Superlattices with AB_4 Stoichiometry Isostructural with Fe_4C. BNSLs isostructural with Fe_4C were formed by 5.8 nm PbSe, 3.0 nm Pd, 7.2 nm PbSe, and 4.2 nm Ag NPs. Figure 9a,b,f represents (100) projections of the Fe_4C-type structure based on a cubic unit cell (SG 215, $P\bar{4}3m$). The unit cell of the Fe_4C lattice and the modeled (100) projection are depicted in panles c and d of Figure 9, respectively. Usually, we observed ~0.5−1 μm^2 defect-free domains with Fe_4C-type ordering. In some samples, Fe_4C structures coexisted with the AB orthorhombic superlattices.

3.6. Binary Superlattices with AB_5 Stoichiometry Isostructural with $CaCu_5$. Slow drying of solutions containing 6.3 nm PbSe and 3.6 nm Ag or 7.2 nm PbSe and 5.0 nm Au NPs dispersed in a tetrachloroethylene−toluene mixture (~1:1 by volume) produced hexagonal superlattices of the $CaCu_5$-type (SG 191, $P6/mmm$). The initial particle concentration ratio was close to 1:7 (large:small). The maximum packing density of $CaCu_5$-type is 0.7 for $\gamma \sim 0.65$. Figure 10 shows the (001) projection of the $CaCu_5$-type structure formed by PbSe and Ag and PbSe and Au NPs. The BNSLs of $CaCu_5$-type were previously observed for 6.3 nm PbSe − 11 nm Fe_2O_3[33] and 2.6 nm − 4.5 nm $CoPt_3$ NPs[35] as well as for large latex particles.[30]

3.7. Binary Superlattices with AB_6 Stoichiometry Isostructural with CaB_6. Being mixed together, 13.4 nm Fe_2O_3 and 5.0 nm Au NPs (particle concentration ratio is ~1:5) show the tendency to form BNSL isostructural with CaB_6 (SG 221, $Pm\bar{3}m$) (Figure 11). The structure of CaB_6 can be described as follows: six small spheres form octahedron which is placed in the center of the cubes; the vertices of those are occupied by four large spheres.

3.8. Binary Superlattices with AB_{13} Stoichiometry. To date, the most complex structure that can self-assemble from hard spheres is the binary superlattice of the $NaZn_{13}$ crystalline type (SG 226, $Fm3c$) (Figure 12). The structure of $NaZn_{13}$ and of several homologous compounds (KZn_{13}, KCd_{13}, etc.) has 112 spheres per unit cell and is defined as follows: each B sphere is surrounded by 12 other B spheres at the vertices of a slightly distorted icosahedron, and each A sphere is surrounded by 24 B spheres at the vertices of a snub cube[52] (Figure 12c). The maximum packing density calculated for AB_{13} with a perfect icosahedron is 0.738.[27] However, a small size distribution of

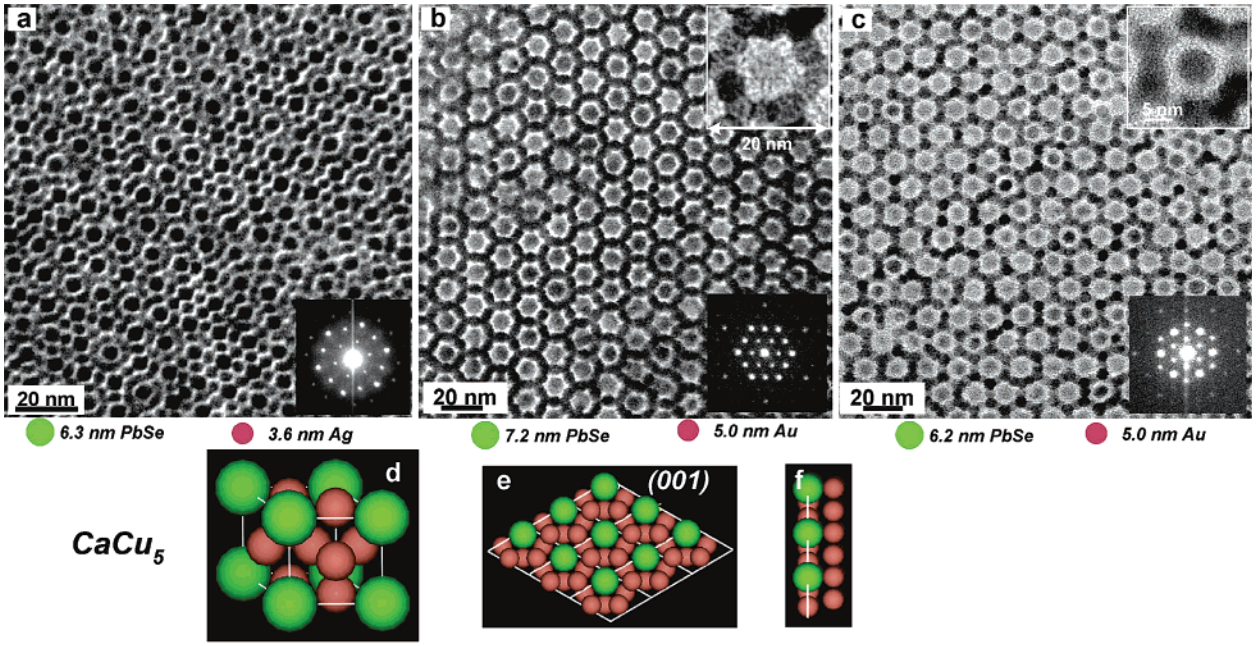

Figure 10. TEM micrographs of BNSL isostructural with $CaCu_5$ formed by (a) 6.3 nm PbSe and 3.6 nm Ag; (b) 7.2 nm PbSe and 5.0 nm Au; (c) 6.2 nm PbSe and 5.0 nm Au NPs; (right bottom insets in a, b, c) Small-angle ED patterns from the (001) projection; (b,c insets) enlarged view of $CaCu_5$-type superlattice consisting of 7.2 nm PbSe and 5.0 nm Au. (d) Three-dimensional sketch of the $CaCu_5$ unit cell. (e) Depiction of the (001) projection. (f) Depiction of minimum number of layers in the (001) projection, leading to the formation of the patterns identical to the observed ones.

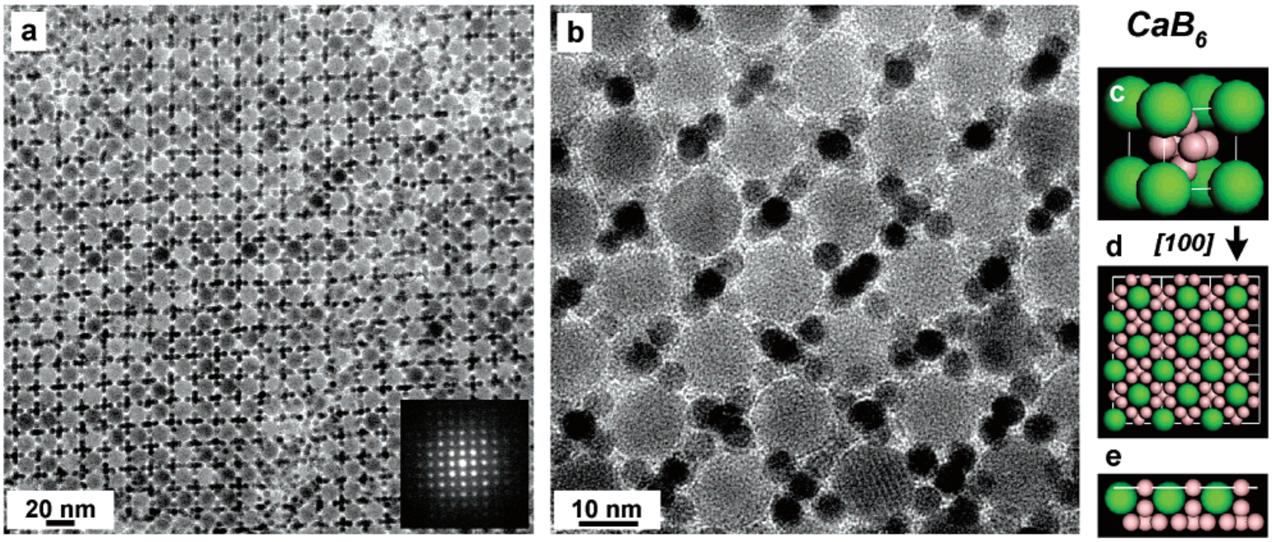

Figure 11. (a) TEM micrograph of a BNSL isostructural with CaB_6 formed by 13.4 nm Fe_2O_3 and 5.0 nm Au NPs; (a, inset) small-angle ED pattern from the (100) projection; (b) enlarged view; (c) 3D sketch of the CaB_6 unit cell. (d) Depiction of the (100) projection. (e) Depiction o minimum number of layers in the (100) projection, leading to the formation of the patterns identical with the observed ones.

the spheres in the icosahedral cluster can increase the packing density. For example, a $NaZn_{13}$ lattice with a slightly smaller central particle in the center of each icosahedron can approach the packing density of ~0.76.[27] Theory predicts stability of a $NaZn_{13}$ lattice built of hard spheres in the range of γ from 0.54 to 0.61 (Table 2). Computer simulations by Frenkel et al.[23] demonstrate that no specific energetic interactions are needed to stabilize such a complex structure and its formation can be supported by an argument based on entropy alone.

Superlattices with $NaZn_{13}$-type structures were first found in natural gem opals[28] and later assembled from latex spheres.[31] Recently, this type of structure was also observed in binary mixture of γ-Fe_2O_3 and PbSe NPs.[33] Figure 12a,b shows the (100) projection of a $NaZn_{13}$-type superlattice consisting of 5.8 nm PbSe and 3.0 nm Pd NPs and 7.2 nm PbSe and 4.2 nm Ag NPs stabilized by oleic acid and dodecanethiol, respectively. The effective particle size ratios are ~0.63 and 0.662, which are above the upper limit of stability range calculated for $NaZn_{13}$.

Because it has the highest packing density, the $NaZn_{13}$ lattice was considered to be the only stable superlattice with AB_{13} stoichiometry. Recently, we demonstrated that $NaZn_{13}$ has a polymorphous form where small particles occupy the vertices of a cuboctahedron (*cub*-AB_{13}).[37] Figure 12e,f shows the (100) projection of *cub*-AB_{13} formed by the same 5.8 nm PbSe and

---

(52) Shoemakker, D.; Marsh, R.; Ewing, F.; Pauling, L. *Acta Crystallogr*. **1952**, *5*, 637−644.

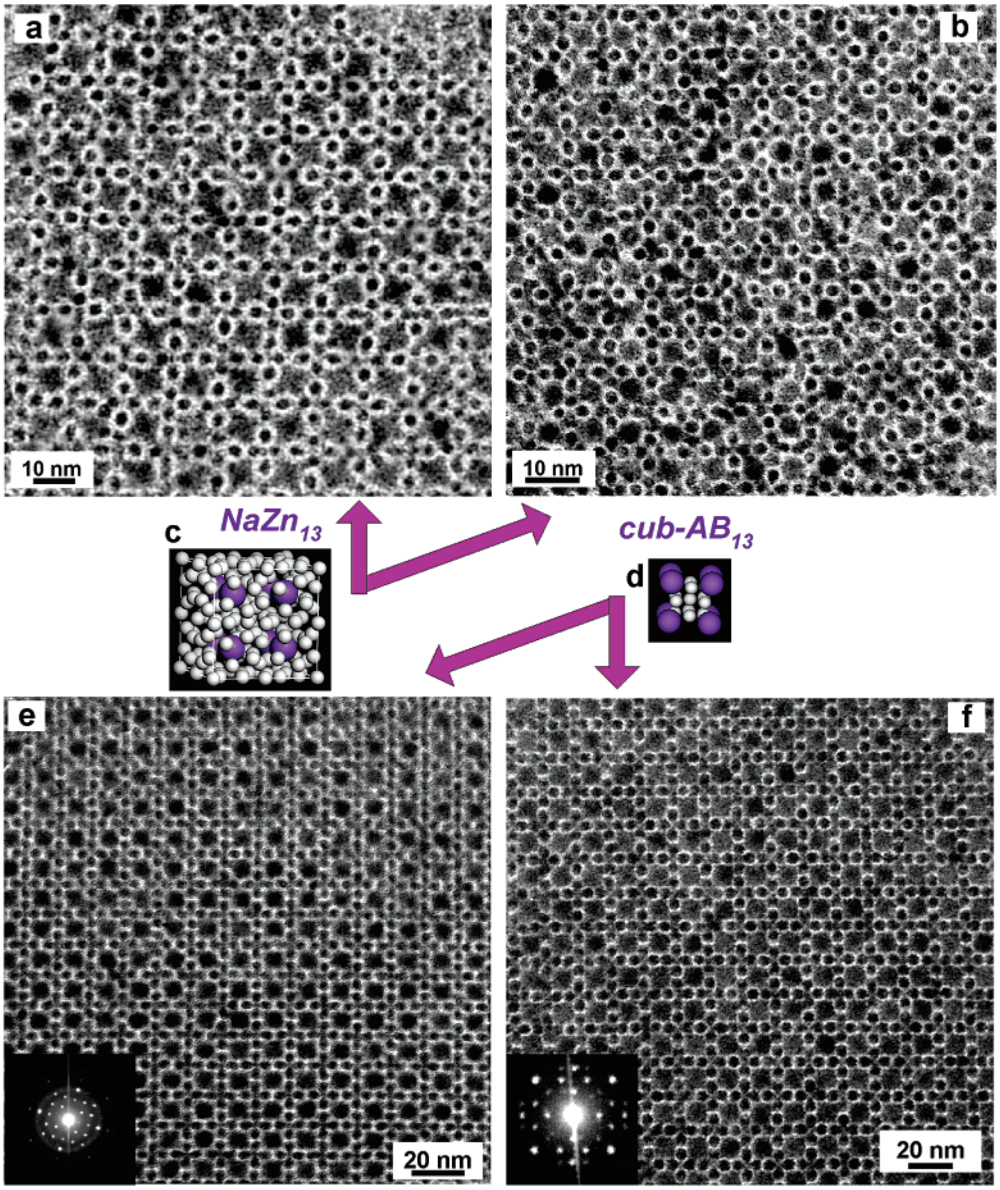

Figure 12. TEM micrographs of (100) projections of BNSL with AB_{13} stoichiometry formed by (a, e) 5.8 nm PbSe and 3.0 nm Pd NPs and (b, f) 7.2 nm PbSe and 4.2 nm Ag NPs: (a, b) BNSL isostructural with $NaZn_{13}$; (e, f) *cub*-AB_{13} superlattice; (c, d) depicting the unit cells of $NaZn_{13}$- and *cub*-AB_{13}-type superlattices, respectively.

3.0 nm Pd and 7.2 nm PbSe and 4.2 nm Ag NPs. The maximum packing density of *cub*-AB_{13} is 0.700. On the other hand, the *cub*-AB_{13} lattice is characterized by a higher number of particle−particle contacts per unit cell. Close particle−particle interactions can be favorable for stabilizing the lattice due to short-range van der Waals' forces.[27] The detailed discussion of both polymorphous forms of AB_{13} nanoparticulate superlattices is reported in ref 37.

3.9. The BNSLs with Unknown Crystallographic Symmetry. In addition to the superlattices that have been assigned by us to well-known crystalline structures, we also observed BNSLs that cannot yet be assigned to specific symmetry groups. For example, Figure 13 demonstrates three superlattices crystallized from the mixtures of PbSe and Pd, Fe_2O_3 and Ag, and Fe_2O_3 and Au NPs. These superstructure as as well as many others not shown in this report give us confidence that the diversity of BNSL presented here is a preview of the materials that will be accessible by this modular assembly approach in a nearest future.

3.10. BNSL Heterostructures. Different types of NP superlattices can form simultaneously on the same substrate. The domains with different symmetry are usually spatially separated. However, sometimes a smooth transition between the two phases is observed. For example, Figure 14a shows an epitaxial "superheterostructure" formed by the (011) planes of AlB_2-type and (100) plane of *cub*-AB_{13}-type superlattices. We assume that the formation of the epitaxial heterostructure can result from a local drop in the concentration Pd NPs during the growth of nanoparticle superlattice. Figure 13b demonstrates the example of the defect heterostructure between the (111) plane of AlB_2-type and the (100) plane of *cub*-AB_{13}-type superlattice, and Figure 13c shows the example of heterostructure formed by the (001) plane of AlB_2-type and the (100) plane of *cub*-AB_{13}-type superlattice. This type of heterostructure can be

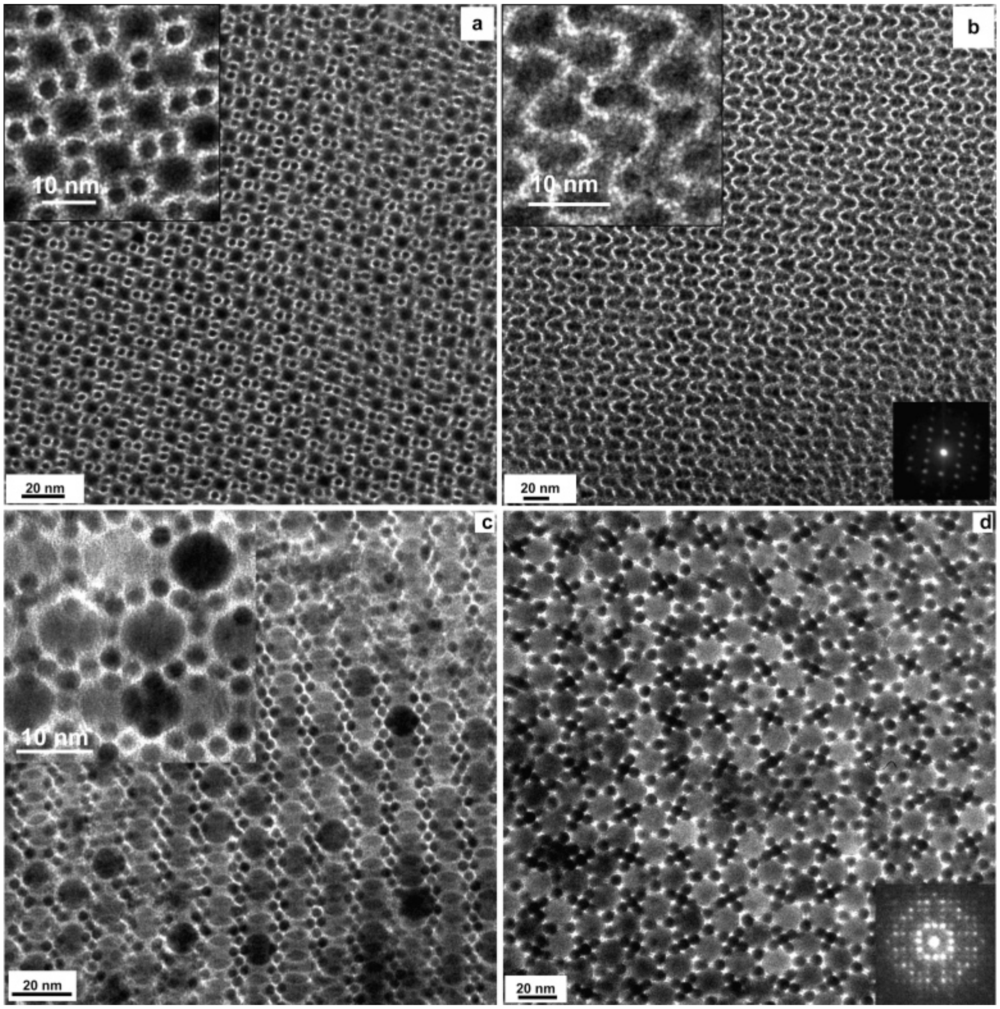

Figure 13. TEM micrographs of "unknown" superstructures formed by (a, b) 6.2 nm PbSe and 3.0 nm Pd NPs; (c) 13.4 nm Fe_2O_3 and 4.2 nm Ag NPs; and (d) 13.4 nm Fe_2O_3 and 5 nm Au NPs.

formed as a collision of laterally growing islands of simultaneously nucleated AlB_2-type and *cub*-AB_{13}-type superlattices. Similar heterostructures were observed by Sanders in Brazilian opals.[29]

3.11. Preferential Orientation of Nanocrystals in BNSLs. Preferred orientation of the atomic lattices of individual nanocrystals packed into a superlattice can be studied by wide-angle selected area electron diffraction (SAED). Randomly oriented nanocrystals result in uniform diffraction rings in wide-angle SAED patterns, as shown in Figure 15a, for a superlattice of 13.4 nm Fe_2O_3 NPs. In contrast, the wide-angle X-ray scattering from Fe_2O_3 NPs packed into the NaCl-type BNSL with 5.5 nm Au NPs (Figure 15d) appears as a series of arcs rather than continuous rings. These arcs originate from the preferential orientation of Fe_2O_3 NPs in the superlattice. Preferential orientation can sometimes be observed in single-component superlattices if nanoparticle shape deviates from spherical due to faceting.[53,54] Figure 15b,c shows examples of preferential orientation in *fcc* arrays of PbSe nanocrystals.

Single-component *fcc* and *hcp* superlattices of nanocrystals usually show unidirectional orientation of atomic lattices, while BNSLs can allow more complex preferential orientation effects. For example, the wide-angle SAED pattern of the (111) plane of NaCl-type Fe_2O_3−Au superlattice shows 12 equidistant arcs for the (220) reflections of Fe_2O_3 NPs (Figure 15d). If all Fe_2O_3 NPs orient in the same direction, we should observe four (220) diffraction spots. The 12 arcs for Fe_2O_3 (220) reflections in the NaCl-type superlattice can result from three different orientations of Fe_2O_3 NPs tilted by 60°.

Preferential orientation can be observed either for a single component of for both components of binary BNSLs. Figure 15e,f shows preferential orientations for both components in PbSe−Au AuCu-type superlattice and Fe_2O_3−PbSe AlB_2-type superlattice, respectively. Figure 15g demonstrates an example of BNSL where the larger 5.8 nm PbSe NPs show preferential orientation while smaller 3.4 nm Ag NPs are disordered. Preferential orientation should be typical for superlattices where the arrangement of nearest neighbors matches the symmetry of nanoparticle facets "locking" each NP in a specific orientation. We have not yet observed preferential orientation effects in orthorombic AB, $CaCu_5$, CaB_6, $NaZn_{13}$, and *cub*-AB_{13} BNSLs.

3.12. Faceting of BNSLs. In the most cases, BNSLs grow as thin extended films. Careful TEM investigation revealed that thicknesses of BNSL films are nearly constant throughout an

---

(53) Zhang, Y.-W.; Sun, X.; Si, R.; You, L.-P.; Yan, C.-H. *J. Am. Chem. Soc.* **2005**, *127*, 360−3261.

(54) Talapin, D. V.; Shevchenko, E. V.; Murray, C. B.; Kornowski, A.; Forster, S.; Weller, H. *J. Am. Chem. Soc.* **2004**, *126*, 12984−12988.

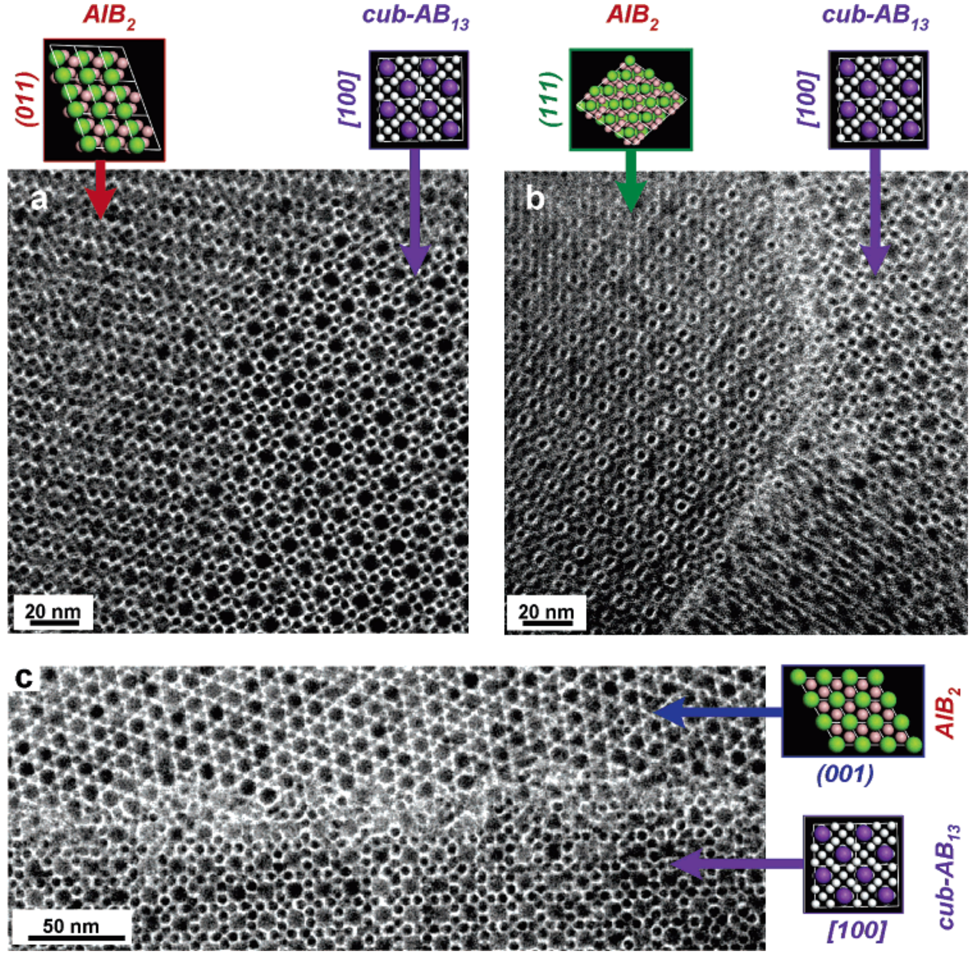

Figure 14. TEM micrograph of (a) the epitaxial “super-heterostructure” formed by the (011) plane of AlB$_2$-type and (100) plane of *cub*-AB$_{13}$-type superlattices; (b) heterostructure formed by the (111) plane of AlB$_2$-type and the (100) plane of *cub*-AB$_{13}$-type superlattices consisting of 5.8 nm PbSe and 3.0 nm Pd NPs, and (c) heterostructure formed by the (001) plane of AlB$_2$-type and the (100) plane of *cub*-AB$_{13}$-type superlattices consisting of 7.2 nm PbSe and 4.2 nm Ag NPs.

entire substrate (a TEM grid), whereas the size of ordered areas becomes larger (~μm^2) as the drying front moves. The surface free energy for different crystallographic faces is usually different.[55] Depending on the type of BNSL, these films are represented by certain, as a rule, low index, crystallographic planes. For instance, in the case of AlB$_2$-type superlattices precipitated onto carbon-coated copper grid, the (001) plane (Figure 5) is dominant over others for almost all studied combinations of nanoparticles, while other planes (Figure 6) are observed in only smaller domains. The growth of BNSL films under conditions discussed above was found to be sensitive to the type of substrate[1] that might indicate the heterogeneous nucleation of BNSLs, a subject to be addressed in future research.

We observed the formation of faceted BNSLs when NPs were self-assembled in the presence of significant excess of oleic acid. These samples needed thorough washing with ethanol before TEM investigation. This procedure removes the excess of oleic acid from the substrate; however, it also led to the partial detachment of the faceted superlattices from the substrate. Figure 16 represents the (001) projection of AlB$_2$-type faceted superlattices. The size of AlB$_2$-type hexagons is in the range of 100−300 nm, which is significantly smaller than the coherent length of ordering in films. Again, as in the case of AlB$_2$-type films, the (001) plane is the most extended in hexagons. This allows us to assume that the (001) facet has the lowest surface free energy.

3.13. General Remarks on BNSL Crystallization. Entropy-driven formation of a crystalline phase in a suspension containing monodisperse hard spheres occurs when the particle volume fraction φ exceeds ~0.49.[56] However, the phase transition in binary mixtures of hard-sphere colloidal particles usually occurs at lower volume fractions[57] because the volume accessible to the small particles increases when two large particles are in a close contact. The resulting gain in the system entropy is considered to be a driving force for clustering of large particles,[58] and as a result, a phase transition occurs. In the case of hard spheres, a binary superlattice can form only if its entropy is higher than the sum of entropies of separated *fcc*-packed small and large spheres. Table 2 summarizes the predicted ranges of stability for different hard-sphere binary superlattices. One can see that stable binary lattices usually have the packing density exceeding the packing density of the *fcc* lattice (~0.7405). This is in agreement with a simple scheme—the higher packing

---

(55) Adamson, A. W.; Gast, A. P. *Physical Chemistry of Surfaces*; John Wiley& Sons: New York, 1997.

(56) Pusey, P. N.; van Megen, W. *Nature* **1986**, *320*, 340−342.

(57) Kaplan, P. D.; Rouke, J. L.; Yodh, G.; Pine, D. J. *Phys. Rev. Lett.* **1994**, *72*, 582−585.

(58) Dijkstra, M.; Frenkel, D.; Hansen, J.-P. *J. Chem. Phys.* **1994**, *101*, 3179−3189.

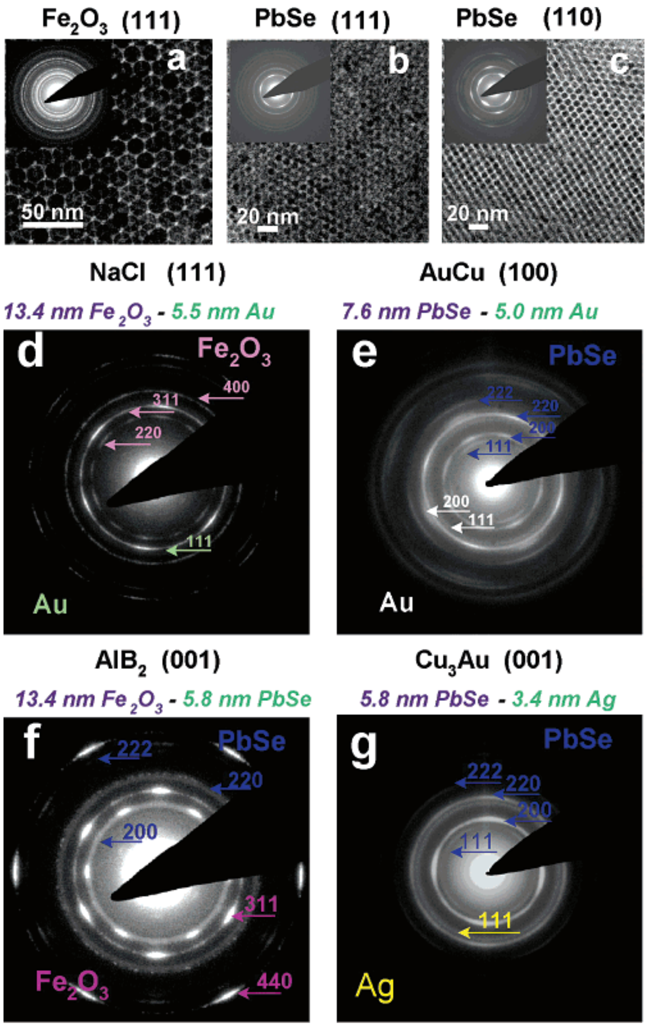

Figure 15. TEM micrographs of (a) the (111) planes of superlattices formed by 13.4 nm Fe_2O_3 NPs; (b) the (111) and (c) (110) planes of superlattices formed by 6.2 nm PbSe NPs. Insets demonstrate the wide-angle selected area ED patterns measured from different planes. (d−g) Wide-angle selected area electron diffraction patterns measured from single-crystal domains of different BNSLs.

density is, the larger excluded volume and, in turn, the higher entropy of the system can be achieved during crystallization of the superlattice.[27] Preliminary predictions of stability for hard-sphere binary superlattices can be drawn by comparison of its packing density with the density of the *fcc* phase. However, the intrinsic entropy of binary superlattice also affects its stability. For example, the maximum packing density of $NaZn_{13}$-type superlattice is slightly below 0.74, while the detailed entropy calculations predict stability of this structure in a rather broad range of γ (Table 2).[23]

The presence of a flat interface (e.g., substrate) can substantially affect crystallization phenomena in binary systems. Crystallization on the wall was observed at particle volume fractions $\varphi \sim 0.2$,[57] that is, well below the values typical for hard-sphere crystallization in the bulk of solution.[56] According to calculations by Frenkel et al.,[61] the presence of a wall can drastically lower the barrier of nucleation and lead to the lateral colloidal crystal (superlattice) growth. These predictions are in agreement with our observation that binary superlattices preferentially grow laterally (Figure S3 from Supporting Information) rather than in all three dimensions. In many cases, the thickness of the superlattices does not exceed one or two unit cells, whereas the lateral size of ordered domains can approach $\sim 10\ \mu m^2$.

Our studies show that the real nanoparticles cannot be approximated by idealized hard spheres. We demonstrated that nanocrystals can self-assemble into a variety of BNSLs with densities significantly smaller than 0.74 (e.g., CuAu, $MgZn_2$, Cu_3Au, Fe_4C, $CaCu_5$, CaB_6, and *cub*-AB_{13}). The low density structures are predicted to be unstable in the case of hard-sphere colloids. However, they do form reproducibly, ruling out the packing density as the major factor in determining stability of binary nanoparticle assemblies.

We recently proposed that self-assembly of BNSLs is driven by Coulomb attraction between oppositely charged nanoparticles in a colloidal solution.[1] Indeed, electrophoretic mobility measurements show that sterically stabilized nanoparticles can hold one or two noncompensated positive or negative elemental charges per particle.[1] The combination of space-filling principle and soft (Coulomb) interparticle interactions can generate a rather complex phase diagram, as it has been recently demonstrated for binary superlattices of charged PMMA beads.[62] However, even the presence of Coulomb interactions cannot explain formation of the entire family of BNSLs reported in this work. We believe that the phase diagram of self-assembled BNSLs is caused by the intrinsic complexity of interactions between nanoscale sterically stabilizied particles. In addition to Coulomb interactions, we should take into account interactions that involve high order moments of charge distribution (i.e., charge−dipole, dipole−dipole, charge-induced dipole, etc.) and dispersive van der Waals forces. In addition to static electric charge, semiconductor nanocrystals can exhibit large dipole moments and polarizabilities;[63−65] large Hamaker constants result in strong van der Waals attraction.[66,67] Table 3 shows estimated magnitudes of the interactions between two 5 nm semiconductor nanocrystals with charge $Z = \pm e$, dipole moments $\mu = 100$ D, and polarizabilities $\alpha/4\pi\epsilon_0 = 30\ nm^3$ (these values are typical for CdSe nanocrystals[63,64]); and two 5 nm metal (e.g., Au) nanoparticles with charge $Z = \pm e$ and polarizabilities $\alpha/4\pi\epsilon_0 = 65\ nm^3$ (~nanoparticle volume). Detailed calculations are given in Supporting Information. One can see that for semiconductors the energy of charge−dipole, dipole−dipole, and charge-induced dipole interactions can approach ~68, 23, and 7% of Coulomb energy, respectively, when the particle separation is ~1 nm (the typical thickness of interdigitated capping ligands). Depending on the orientation of the nanoparticle dipole moments, these additional terms can double (or cancel) electrostatic interactions between adjacent nanoparticles in the BNSL. This situation is quite unique. For example, for charged small molecules, the Coulomb interactions

---

(59) Hunt, N.; Jardine, R.; Bartlett, P. *Phys. Rev. E* **2000**, *62*, 900−913.
(60) Schofield, A. B. *Phys. Rev. E* **2001**, *64*, 051403−051406.
(61) Auer, S.; Frenkel, D. *Phys. Rev. Lett.* **2003**, *91*, 015703−1−015703−4.
(62) Leunissen, M. E.; Christova, C. G.; Hynninen, A.-P.; Royall, C. P.; Campbell, A. I.; Imhof, A.; Dijkstra, M.; van Roij, R.; van Blaaderen, A. *Nature* **2005**, *437*, 235−240.
(63) Shim, M.; Guyot-Sionnest, P. *J. Chem. Phys.* **1999**, *111*, 6955−6964.
(64) Li, L.-S.; Alivisatos, A. P. *Phys. Rev. Lett.* **2003**, *90*, 097402−1−097402−4.
(65) Rabani, E.; Hetényi, B.; Berne, B. J.; Brus, L. E. *J. Chem. Phys.* **1999**, *110*, 5355−5369.
(66) Hamaker, H. C. *Physica* **1937**, *4*, 1058−1072.
(67) Ohara, P. C.; Leff, D. V.; Heath, J. R.; Gelbart, W. M. *Phys. Rev. Lett.* **1995**, *75*, 3466−3469.

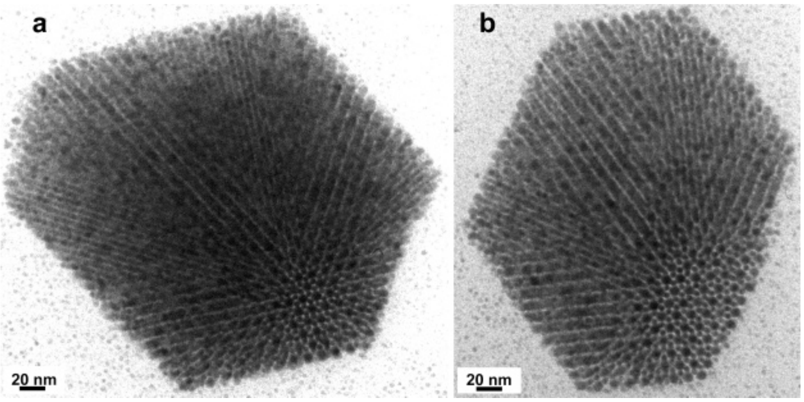

Figure 16. TEM micrographs of faceted AlB_2-type BNSLs formed by 7.2 nm PbSe and 4.2 nm Ag NPs.

Table 3. Magnitudes of Interactions between Two 5 nm Nanoparticles with Charges $Z = \pm e$ and Dipoles Oriented along the Particle−Particle Axis (R is the particle center-to-center distance)

interaction	$V_{\text{semiconductor − semiconductor}}$ [eV] $R = 6$ nm	$V_{\text{semiconductor − semiconductor}}$ [eV] $R = 10$ nm	$V_{\text{metal − metal}}$ [eV] $R = 6$ nm	$V_{\text{metal − metal}}$ [eV] $R = 10$ nm
Coulomb ($\sim 1/R$)	0.12	0.072	0.12	0.072
charge−dipole ($\sim 1/R^2$)	0.082	0.029		
dipole−dipole ($\sim 1/R^3$)	0.028	5.8×10^{-3}		
charge−ind. dipole ($\sim 1/R^4$)	8.4×10^{-3}	1.1×10^{-3}	0.018	2.3×10^{-3}
van der Waals ($\sim 1/R^6$)	0.016	2.1×10^{-4}	0.097	1.3×10^{-3}

dominate over dipolar and dispersive interactions by orders of magnitude.[68]

Dispersive (van der Waals) potential between two nanoparticles of radii R_A and R_B at the distance of closest approach D can be calculated from direct pairwise summation over atomic dispersional attractions proportional to $-1/R^6$:[66,67]

$$V^{\mathrm{vdW}} = -\frac{A}{12}\left\{\frac{S}{D[1 + D/2(R_A + R_B)]} + \frac{1}{1 + D/S + D^2/4R_AR_B} + 2\ln\left(\frac{D[1 + D/2(R_A + R_B)]}{R[1 + D/S + D^2/4R_AR_B]}\right)\right\} = -\frac{A}{12}\xi(R_A,R_B,D) \quad (1)$$

where A is the solvent-retarded Hamaker constant and $S = 2R_AR_B/(R_A + R_B)$ is the reduced radius.

The van der Waals energy can vary substantially for different materials. Thus, $A \sim 3.1 \times 10^{-19}$ J ($\sim$1.95 eV) for Au−Au attraction through a hydrocarbon layer[69,70] (some authors reported larger values, e.g., 3 eV[71]), whereas CdSe−CdSe attraction is significantly weaker: $A \sim 5 \times 10^{-20}$ J ($\sim$0.32 eV).[7271−72] The contribution of dispersive interactions to the pair potential is relatively small ($\sim$13% of the Coulomb energy) for 5 nm semiconductor nanoparticles at $R = 6$ nm (Table 3). However, in the case of metals (Au, Ag, Pd), van der Waals energy can rival the Coulomb potential at small interparticle separations. In solvents with a high dielectric constant (e.g., chloroform), dispersive interactions can cause short-range attraction between oddly charged metal nanoparticles. At very small interparticle distances ($<\sim$1−1.5 nm), the pair potential will be dominated by repulsion between the nanoparticle ligands that can be described by osmotic and sterical terms[73] (see Supporting Information for details).

All these interactions contribute to the total potential energy of a BNSL. Depending on the averaging effects, the interactions discussed above can contribute to the pair potential and the superlattice binding energy with different weight. To demonstrate this, we calculated Coulomb and van der Waals binding energies for the NaCl-type BNSL assembled of oppositely charged 13.4 nm Fe_2O_3 and 5.0 nm Au nanoparticles (Figure 2a).

The Coulomb binding energy of an AB_x-type BNSL can be calculated as $U_{\text{Coulomb}} \approx MZ_AZ_Be^2/(4\pi\epsilon\epsilon_0R_0)$per AB_x “molecule”, where M is the Madelung constant and R_0 is the nearest-neighbor center-to-center distance. For the Fe_2O_3−Au BNSL shown in Figure 2a, $R_0 = 11.5$ nm, $M_{\text{NaCl}} = -1.7476$. and $U_{\text{Coulomb}} \approx -0.1$ eV per unit cell, assuming one elemental charge per particle and $\epsilon = 2$.[1]

The van der Waals binding energy (U_{vdW}) for a BNSL assembled from nanoparticles with radii R_A and R_B was estimated by summation of V_{ij}^{vdW} over all nanoparticles in the superlattice:

$$U_{\text{vdW}} = \frac{1}{2}\sum_i\sum_j V_{ij}^{\text{vdW}} = -\frac{1}{24}\sum_i\sum_j A_{ij}\xi(R_i,R_j,D_{ij}) \quad (2)$$

In a NaCl-type binary superlattice, each particle A has 6 particles B at the nearest-neighbor distance R_0, 12 particles A at $\sqrt{2}R_0$, 8 particles B at $\sqrt{3}R_0$, 6 particles A at $2R_0$, 24 particles B at $\sqrt{5}R_0$, and so forth. For a superlattice of $2N$ nanoparticles (or N unit cells), the sum (eq 3) can be calculated as

$$U_{\text{vdW}} = -\frac{N}{24}\left[\sum_j\{A_{ij}\xi(R_i,R_j,D_{ij})\}_{i=\text{particleA}} + \sum_j\{A_{ij}\xi(R_i,R_j,D_{ij})\}_{i=\text{particleB}}\right] = -\frac{N}{2}\left[A_{AB}\xi(R_A,R_B,D_0) + A_{AA}\xi(R_A,R_A,D_1) + A_{BB}\xi(R_B,R_B,D_1) + \frac{4}{3}A_{AB}\xi(R_A,R_B,D_2) + \cdots\right] \quad (3)$$

where A_{AA}, A_{BB}, and A_{AB} are the Hamaker constants for

---

(68) Berry, R. S.; Rice, S. A.; Ross, J. *Physical Chemistry*; Oxford University Press: New York, 2000.
(69) Bargeman, D.; van Voorst Vader, F. *J. Electroanal. Chem.* **1972**, *37*, 45−52.
(70) Bergström, L. *Adv. Colloid Interface Sci.* **1997**, *70*, 125−169.
(71) Saunders, A. E.; Korgel, B. A. *J. Phys. Chem. B* **2004**, *108*, 16732−16738.
(72) Ge, G.; Brus, L. *J. Phys. Chem. B* **2000**, *104*, 9573−9575.

interactions between two particles of type A, two particles of type B, and particle A with particle B, respectively; $D_k = \sqrt{(k+1)}R_0 - R_i - R_j$.

Due to the short-range nature of dispersive interactions, V_{ij}^{vdW} quickly decays with increasing D and the series (eq 3) rapidly converges. For the BNSL shown in Figure 2a ($R_A = 6.7$ nm, $R_B = 2.5$ nm, $R_0 = 11.5$ nm, and $D_0 = 2.3$ nm), to a good approximation, we can neglect contributions from nanoparticles at distances $> \sqrt{3}R_0$. In this case

$$U_{\mathrm{vdW}} \approx -N[0.119A_{\mathrm{AB}} + 0.261A_{\mathrm{AA}} + 1.632 \times 10^{-4}A_{\mathrm{BB}}] \qquad (4)$$

Hamaker constant for gold−gold attraction through a hydrocarbon medium is $A_{\mathrm{BB}} \sim 3.1 \times 10^{-19}$ J (~1.95 eV).[69] We found a large spread in reported Hamaker constant values for Fe_2O_3−Fe_2O_3 attraction in aqueous medium, the reported values varied from 1×10^{-20} to 1×10^{-19} J (0.06−0.6 eV).[70,74,75] Hamaker constants in hydrocarbon medium are generally lower than Hamaker constants in water [D9], and we used 3×10^{-20} J (0.19 eV) as the realistic estimate for A_{AA}. This value fits well to the general trend observed for transition metal oxides.[76] The Hamaker constant for the Au−Fe_2O_3 interaction through hydrocarbon medium has not been measured, and we estimated it as $[A_{\mathrm{AA}}A_{\mathrm{BB}}]^{1/2} \sim 1 \times 10^{-19}$ J (0.6 eV).[76] Substituting Hamaker constants into eq 4 gives the van der Waals energy of ~ -0.12 eV per unit cell. U_{vdW} is comparable (exceeds by ~20%) to U_{Coulomb}, despite $V^{\mathrm{vdW}} < V^{\mathrm{Coulomb}}$ in the pair potentials. This is because the dispersive interactions are attractive, whereas the Coulomb interactions can be both attractive and repulsive. Competition between Coulomb and van der Waals forces can stabilize a variety of complex BNSL structures. Thus, formation of BNSLs containing close-packed clusters of metal nanoparticles, such as Fe_4C (Figure 9), $CaCu_5$ (Figure 10), CaB_6 (Figure 11), $NaZn_{13}$, and *cub*-AB_{13} (Figure 12), should be energetically favorable because of strong van der Waals attraction between metal nanoparticles in these clusters (Ag, Au, Pd). Additionally, ordering of dipole moments of semiconductor nanocrystal should significantly affect the total BNSL binding energy.

It was also shown that surfactants can influence the assembly of NPs.[77] Thus, $Au_{140}(C_{12}H_{25}S)_{62}$ clusters capped with long-chain thiols are predicted to pack into a 3D tetragonal superlattice, whereas $Au_{140}(C_4H_9S)_{62}$ should form a *bcc* superlattice.[77] Another factor that might affect the packing symmetry is the deviation of NP shape from spherical.[27] The shape of crystalline NPs is usually determined by nanocrystal faceting.[78] The highest packing density and stronger van der Waals attraction of faceted nanocrystals are achieved if the packing symmetry reflects the shape of the NP building blocks.

Energetic factors discussed above affect the relative stability of different binary superlattices. Additionally, the kinetics of superlattice nucleation and growth could be responsible for the preferential growth of some superstructures over the others. For example, easier nucleation of relatively simple and highly symmetric *cub*-AB_{13} superlattices might explain why this structure can dominate over the denser and, potentially, more stable $NaZn_{13}$-type superlattice.[37] Finite size distribution is always present in nanoparticle samples, and this could have a substantial influence on both thermodynamics and kinetics of formation of BNSL. Murray and Sanders calculated that a slight distribution in the size of small particles can increase the packing density of $NaZn_{13}$-type superlattice from 0.738 to 0.760.[27] The size distribution of NPs used in this work for growing binary superlattices was ~5−8%. We observed suppression of crystallization from mixtures containing particles with broad size distribution (> ~14% standard deviation). Notably smaller fragments (~400 nm^2) of binary superlattices could sometimes grow from solutions of NPs with polydispersity of ~10−12% standard deviation. These results are in qualitative agreement with numerical calculations[79] predicting suppression of nucleation in mixtures of polydisperse hard spheres. Further studies are necessary to reveal the combination of thermodynamic and kinetic factors affecting the nucleation and growth of binary superlattices.

4. Concluding Remarks

We have induced a wide array of monodisperse metal, semiconductor, and magnetic nanocrystals to self-assemble into binary nanocrystal superlattices (BNSLs), yielding a broad new class of multifunctional nanocomposites. Superlattices with AB, AB_2, AB_3, AB_4, AB_5, AB_6, and AB_{13} stoichiometries and cubic, hexagonal, tetragonal, and orthorhombic symmetries have all been identified. We have established a combination of electron microscopy, diffraction, and structural modeling as a methodology for the systematic classification and characterization of BNSLs. The richness and diversity of binary superstructures presents a challenge to both experimentalists and theorists to understand the principles that guide assembly at the nanoscale level. We demonstrate that BNSL formation is guided by a combination of competing short-range Coulonbic, dipolar, and van der Waals interactions. We predict that novel systems could enable fundamental studies of nucleation and growth of complex crystals. This report demonstrates only a fraction of the structures that might self-assemble from multicomponent mixtures of nanoparticles, and we feel that this modular approach to nanomaterials design will have great potential for a rational design of complex nanoscale materials.

Acknowledgment. We wish to thank Prof. Daan Frenkel (FOM-Institute for Atomic and Molecular Physics, Netherlands), Dr. Glenn Held (T. J. Watson Research Center, IBM), Prof. Louis Brus, and Prof. Irving Herman (Columbia University) for helpful discussions, and Robert Sandstrom (T. J. Watson Research Center, IBM) for technical support. This work was supported primarily by the MRSEC Program of the National Science Foundation under Award Number DMR-0213574, by the New York State Office of Science, Technology and Academic Research (NYSTAR), and in part by the Department of Energy, Office of Basic Energy Sciences, Grant DE-FG02-03ER15463. S.O. is grateful for support from an NSF CAREER award, DMR-0348938.

Supporting Information Available: Unit cell and modeled (001) plane of CaF_2-type superlattice (Figure S1). TEM

---

(73) Rabideau, B. D.; Bonnecaze, R. T. *Langmuir* **2005**, *21*, 10856−10861.
(74) Mylon, S. E.; Chen, K. L.; Elimelech, M. *Langmuir* **2004**, *20*, 9000−9006.
(75) Lyklema, J. *Fundamentals of Colloid and Interface Science*; Academic Press: London, 1993; Vol. I.
(76) French, R. H. *J. Am. Ceram. Soc.* **2000**, *83*, 2117−2146.
(77) Luedtke, W. D.; Landman, U. *J. Phys. Chem.* **1996**, *100*, 13323−13329.
(78) Wang, Z. L. *Adv. Mater.* **1998**, *10*, 13−30.
(79) Auer, S.; Frenkel, D. *Nature* **2001**, *413*, 711−713.

micrographs of the hexagonal $MgNi_2$-type superlattice, modeled unit cell, and projections of this structure (Figure S2). TEM overviews demonstrating the lateral growth of nanoparticulate superlattices (Figure S3). Sketch of charge−dipole and dipole−dipole nanoparticle interactions (Figure S4). Typical pair potentials between two oddly, evenly charged dielectric (semiconducting) and between two evenly and oddly charged metal nanoparticles with charges $Z = \pm e$ (Figure S5). This material is available free of charge via the Internet at http://pubs.acs.org.

JA0564261